



A glucose-like metabolite deficient in diabetes inhibits cellular entry of SARS-CoV-2

Liangqin Tong^{1,2,3,13}, Xiaoping Xiao^{1,2,3,13}, Min Li^{4,13}, Shisong Fang^{2,13}, Enhao Ma¹, Xi Yu¹, Yibin Zhu¹, Chunli Wu², Deyu Tian⁵, Fan Yang², Jing Sun⁶, Jing Qu², Nianzhen Zheng^{7,8}, Shumin Liao⁸, Wanbo Tai³, Shengyong Feng¹, Liming Zhang¹, Yuhan Li¹, Lin Wang¹, Xuelian Han⁴, Shihui Sun⁴, Long Yang⁹, Hui Zhong¹⁰, Jincun Zhao⁶, Wenjun Liu⁵, Xiaohui Liu¹¹, Penghua Wang¹², Liang Li^{7,8}, Guangyu Zhao⁴, Renli Zhang² and Gong Cheng^{1,2,3}

The severity and mortality of COVID-19 are associated with pre-existing medical comorbidities such as diabetes mellitus. However, the underlying causes for increased susceptibility to viral infection in patients with diabetes is not fully understood. Here we identify several small-molecule metabolites from human blood with effective antiviral activity against SARS-CoV-2, one of which, 1,5-anhydro-D-glucitol (1,5-AG), is associated with diabetes mellitus. The serum 1,5-AG level is significantly lower in patients with diabetes. In vitro, the level of SARS-CoV-2 replication is higher in the presence of serum from patients with diabetes than from healthy individuals and this is counteracted by supplementation of 1,5-AG to the serum from patients. Diabetic (db/db) mice undergo SARS-CoV-2 infection accompanied by much higher viral loads and more severe respiratory tissue damage when compared to wild-type mice. Sustained supplementation of 1,5-AG in diabetic mice reduces SARS-CoV-2 loads and disease severity to similar levels in nondiabetic mice. Mechanistically, 1,5-AG directly binds the S2 subunit of the SARS-CoV-2 spike protein, thereby interrupting spike-mediated virus-host membrane fusion. Our results reveal a mechanism that contributes to COVID-19 pathogenesis in the diabetic population and suggest that 1,5-AG supplementation may be beneficial to diabetic patients against severe COVID-19.

The outcomes of a viral infection and disease progression are determined by complex host–virus interactions^{1,2}. Infection with severe acute respiratory syndrome coronavirus-2 (SARS-CoV-2), the etiological agent of coronavirus disease 2019 (COVID-19), presents highly heterogeneous clinical manifestations in humans^{3,4}. The majority of individuals infected with SARS-CoV-2 have asymptomatic, mild or moderate disease; however, elderly individuals and patients with comorbidities such as type 2 diabetes mellitus are at a much higher risk of serious illness and even death⁵. Although complex immunological changes may underlie the vulnerability of these

populations, metabolic disorders are also evident in patients with comorbidities^{5,6} and could predispose them to severe viral infections^{5,7}. Nonetheless, the role of metabolic factors in COVID-19 pathogenesis is still largely unknown.

Serum metabolites vary significantly in terms of quantity and compositions among individuals⁸. Therefore, we assessed whether the metabolites in human serum might regulate SARS-CoV-2 infection. Human serum samples were separated by centrifugation with a 3-kDa filter. Either the filtrates containing small-molecule metabolites or the upper retentate with serum proteins was incubated with Vero cells and infected with SARS-CoV-2 (Fig. 1a and Supplementary Table 1a). The amount of viral RNA was significantly reduced in cells treated with the serum filtrates compared to the infected control (Fig. 1b). Notably, incubation with the upper retentate also impaired viral infection, which may be attributed to virucidal proteinaceous factors, such as complements⁹ (Fig. 1b). We next aimed to identify the metabolic component(s) with antiviral activity in human serum. A total 484 metabolite compounds, which were pooled from either our experiment of three donors or a published metabolites profile¹⁰ (Supplementary Table 1b), were filtered using the Human Metabolome Database (HMDB) (<https://hmdb.ca>). A total of 298 small-molecule metabolites were identified for further investigation; notably, 222 were commercially available (Fig. 1c and Supplementary Table 2). We incubated Vero cells with 100 μ M solutions of each metabolite and then infected them with SARS-CoV-2. Seven metabolites reduced the amount of viral RNA with an inhibition rate higher than 95% (Fig. 1d). *N*-oleoyl glycine was excluded from further analyses because of its potent cytotoxicity (Extended Data Fig. 1a). The antiviral activity of the remaining six metabolites was validated by immunofluorescence staining with a monoclonal antibody against the SARS-CoV-2 nucleocapsid (N) (Fig. 1e(i),(ii)). The 50% maximal inhibitory concentration (IC₅₀) of these metabolites ranged from 7.18 μ M to 43.10 μ M in Vero cells (Fig. 1f). Three metabolites,

¹Tsinghua-Peking Joint Center for Life Sciences, School of Medicine, Tsinghua University, Beijing, China. ²Institute of Pathogenic Organisms, Shenzhen Center for Disease Control and Prevention, Shenzhen, China. ³Institute of Infectious Diseases, Shenzhen Bay Laboratory, Shenzhen, China. ⁴State Key Laboratory of Pathogen and Biosecurity, Beijing Institute of Microbiology and Epidemiology, Academy of Military Medical Sciences, Beijing, China. ⁵CAS Key Laboratory of Pathogenic Microbiology and Immunology, Institute of Microbiology, Chinese Academy of Sciences, Beijing, China. ⁶State Key Laboratory of Respiratory Disease, National Clinical Research Center for Respiratory Disease, Guangzhou Institute of Respiratory Health, the First Affiliated Hospital of Guangzhou Medical University, Guangzhou, China. ⁷Department of Pharmacology, School of Medicine, Southern University of Science and Technology, Shenzhen, China. ⁸Shenzhen Institutes of Advanced Technology, Chinese Academy of Sciences, Shenzhen, China. ⁹School of Integrative Medicine, Tianjin University of Traditional Chinese Medicine, Tianjin, China. ¹⁰Beijing Institute of Biotechnology, Academy of Military Medical Sciences, Beijing, China. ¹¹School of Life Science, Tsinghua University, Beijing, China. ¹²Department of Immunology, School of Medicine, the University of Connecticut Health Center, Farmington, CT, USA. ¹³These authors contributed equally: Liangqin Tong, Xiaoping Xiao, Min Li, Shisong Fang. ✉e-mail: lil@sustech.edu.cn; guangyu0525@163.com; renlizhangszcdc@aliyun.com; gongcheng@mail.tsinghua.edu.cn

1,5-AG, chenodeoxycholic acid (CDCA) and 5-methoxytryptophol (5-MT), are known as endogenous metabolites that can be synthesized by human cells^{11–14}. Ellagic acid, 1-naphthol, 1,5-AG and 4-hydroxyretinoic acid (4-HA) are exogenous serum metabolites that may be acquired from food sources^{15–18} (Fig. 1g).

We next examined the potential roles of these endogenous metabolites to investigate the interplay between host metabolism and SARS-CoV-2 infection. Diabetes mellitus is a high risk factor for severe COVID-19 (refs. 7,19). We investigated whether the levels of endogenous metabolites were correlated with and accounted for the differential antiviral activities between the healthy and diabetic groups. The serum samples were collected and characterized according to the diagnostic criteria for diabetes by the World Health Organization²⁰. The significant increase in fasting glucose indicated that the serum from patients with diabetes was tied to hyperglycemia (Extended Data Fig. 1b and Supplementary Table 1c,d). In fact, we found that the 1,5-AG serum level was much lower in patients with diabetes than that in healthy donors (Fig. 2a), whereas the CDCA (Extended Data Fig. 1c) and 5-MT levels (Extended Data Fig. 1d) were not. Indeed, 1,5-AG is a well-established blood biomarker for human diabetes mellitus. The urinary excretion of 1,5-AG is increased by the competitive inhibition of glucose in patients with diabetes with glycosuria, resulting in a significant reduction of 1,5-AG in the serum of patients with diabetes²¹. The normal physiological concentration of 1,5-AG ranges from 28 to 367 μM in human serum²². The 1,5-AG concentration was reduced by 5–10 times in the serum of individuals with diabetes compared to that of healthy controls (Fig. 2a). The amount of viral RNA was much higher in Vero cells treated with the sera from patients with diabetes than in cells treated with sera from healthy donors. Notably, 1,5-AG supplementation of the sera from patients with diabetes reduced the amount of viral RNA (Fig. 2b). We next assessed the antiviral effect of 1,5-AG on a human colon carcinoma cell line (Caco-2) that is susceptible to SARS-CoV-2 (ref. 23). Incubation with 1,5-AG reduced SARS-CoV-2 replication in a dose-dependent manner (Fig. 2c). The antiviral activity of 1,5-AG in Caco-2 cells was further validated by western blotting (Fig. 2d) and immunofluorescence staining (Fig. 2e). Consistently, 1,5-AG treatment decreased the amount of viral nucleocapsid in the supernatant of the Caco-2 cells, as detected by enzyme-linked immunosorbent assay (ELISA) (Fig. 2f). The Caco-2 cells maintained normal viability under the experimental settings of 1,5-AG incubation, which was assessed by a Cell Counting Kit-8 (CCK-8) assay (Extended Data Fig. 1e). Altogether, these results indicate that 1,5-AG is an effective anti-SARS-CoV-2 serum metabolite that is downregulated by diabetes.

In addition to the blood, 1,5-AG is maintained at a steady level in various organs^{11,24}. As SARS-CoV-2 infects the epithelial cells

that line the surface of the respiratory tract, we therefore assessed the concentration of 1,5-AG in mouse bronchoalveolar lavage fluid (BALF), which is related to the presence of 1,5-AG on the surface of COVID-19-target tissues^{25,26}. Notably, there was 6–12 μM 1,5-AG detected in the BALF collected from 500 μl of PBS fluid squirted into the mouse lung (Extended Data Fig. 1f). As the volume of alveolar epithelial lining liquid was estimated to be 10 μl in mice²⁷, the approximate concentration of 1,5-AG was 450 μM in mice alveolar liquid. Thus, we tested the antiviral effect of 1,5-AG on a human air–liquid interface (ALI) epithelial culture of the lower respiratory tract. Epithelial culture of bronchoscopy was derived from patient biopsies^{28,29} (Supplementary Table 1e). The differentiated bronchiolar epithelium was detected by staining for a specific surface marker in ciliated columnar cells, goblet cells and basal cells (Fig. 2g). In fact, the viability of cells from bronchiolar epithelial cultures was not influenced by serial of 1,5-AG incubation (Extended Data Fig. 1g). Incubation with 1,5-AG reduced the amount of viral RNA in the supernatant (Fig. 2h) and tissue (Fig. 2i) of human bronchiolar epithelial cultures in a dose-dependent manner. A marked decrease in viral infection was recorded in the 1,5-AG-treated epithelium as detected by an immunofluorescence assay (Fig. 2j).

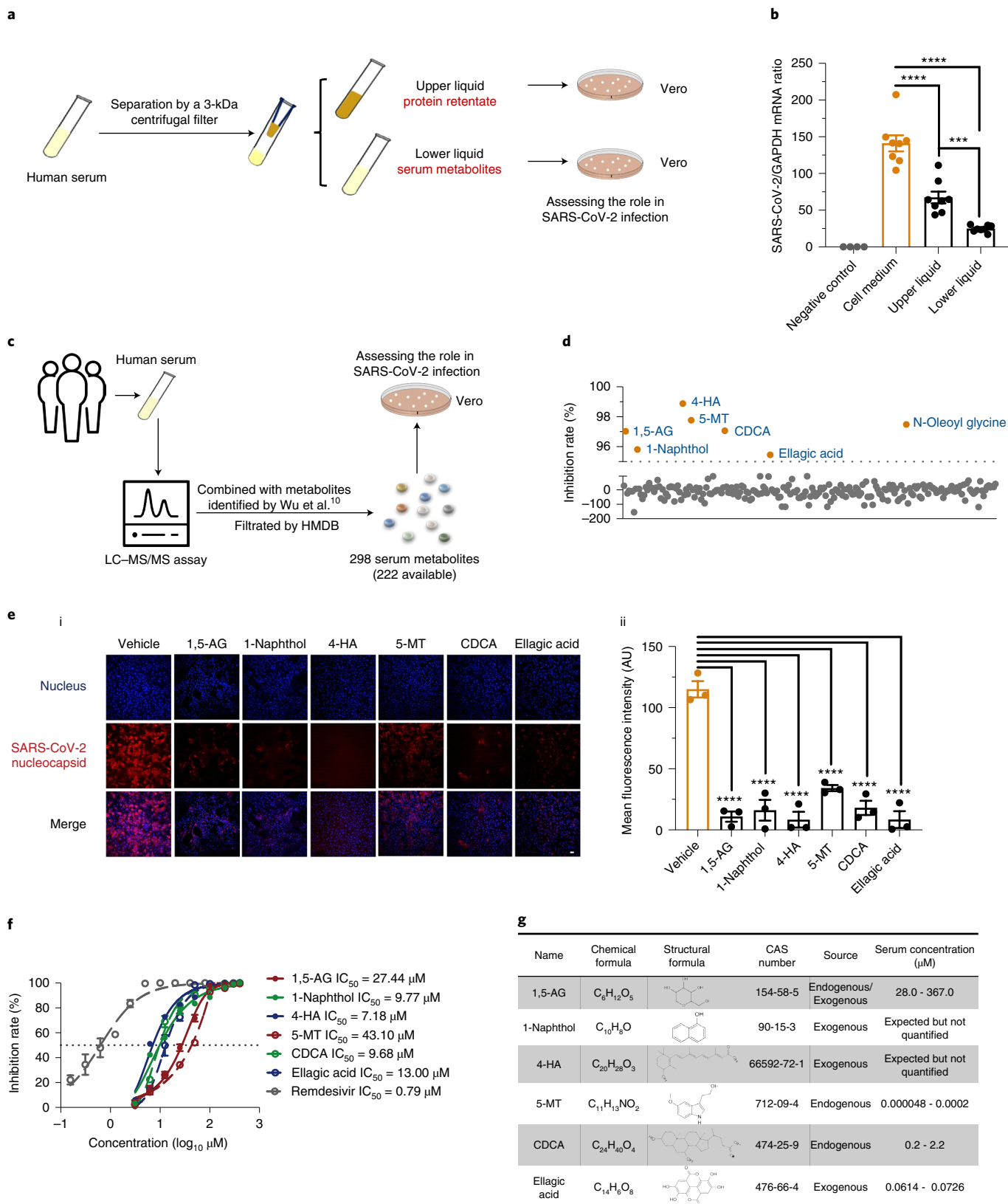
Next, we investigated the mechanism by which 1,5-AG resists SARS-CoV-2 infection. 1,5-AG is a glucose-like pyranoid polyol³⁰. A recent study suggested that elevated glucose levels and sustained aerobic glycolysis in human monocytes directly promote SARS-CoV-2 infection³¹. Nonetheless, treating with 1,5-AG did not affect the glycolysis, glycolytic capacity or glycolytic reserve in the Vero cells (Extended Data Fig. 2a–e). To assess the stage of SARS-CoV-2 infection inhibited by 1,5-AG, we treated Caco-2 cells with 1,5-AG 1 h before (pre), simultaneously with (co), or 1 h after (post) SARS-CoV-2 inoculation to further identify the stage of SARS-CoV-2 infection in which 1,5-AG acts (Fig. 3a). The post-treatment showed no effect, while the pre-treatment slightly reduced the amount of viral RNA. Notably, the co-treatment led to a dramatic reduction in the amount of viral RNA (Fig. 3b), indicating that 1,5-AG may exert its maximal antiviral effect during viral entry. We next assessed the effect of 1,5-AG on SARS-CoV-2 attachment and internalization to confirm this finding. SARS-CoV-2 was incubated with Caco-2 cells at 4 °C for 1 h in the presence or absence of 1,5-AG to allow viral attachment but not internalization into host cells³² and unbound virions were then removed by extensive washing with ice-cold PBS. 1,5-AG does not interfere with SARS-CoV-2 attachment to host cells (Fig. 3c, left). Nonetheless, the viral internalization was significantly reduced by 1,5-AG treatment in a dose-dependent manner (Fig. 3c, right). Moreover, 1,5-AG did not directly block the interaction between the spike protein and hACE2 (Extended Data Fig. 2f).

Fig. 1 | Screening of human serum metabolites against SARS-CoV-2 infection. a,b, Roles of human serum metabolites in SARS-CoV-2 infection.

Schematic diagram of the study design (a). Incubation with human serum-derived filtrates impaired SARS-CoV-2 replication (b). Negative control: cells incubated with cell medium without SARS-CoV-2 infection. For the upper liquid group and lower liquid group, each dot represents one donor ($n=8$ healthy donors). $P=0.0001$ for upper liquid versus lower liquid, $P<0.0001$ for cell medium versus upper liquid, cell medium versus lower liquid. **c,d**, Identification of the human serum metabolite(s) that prevent SARS-CoV-2 infection. Schematic diagram of the screening experimental design (c). The role of human serum metabolite(s) in SARS-CoV-2 infection (d). The amount of viral RNA was normalized to human *GAPDH*. The dot is the mean value. **e**, Assessing the antiviral activities of six metabolites from human serum by immunofluorescence staining. The nucleocapsid was stained with Alexa Fluor 546-conjugated anti-rabbit IgG (red). The nuclei were stained with To-Pro-3 iodide (blue). The stained cells were examined using a Zeiss LSM 880 meta confocal microscope in multitrack mode (i). Representative of three confocal immunofluorescence images from three biological replicates was shown. Scale bars, 20 μm . (ii) Mean fluorescence intensity in differently treated cells. Three images stained with nucleocapsid and Alexa Fluor 546-conjugated anti-rabbit IgG individually selected from three biological replicates were used to determine the mean fluorescence intensity with ImageJ (National Institutes of Health). AU, arbitrary units. $P<0.0001$ for vehicle versus 1,5-AG, vehicle versus 1-naphthol, vehicle versus 4-HA, vehicle versus 5-MT, vehicle versus CDCA, vehicle versus ellagic acid. **f,g**, Measurement of the half maximal inhibitory concentration (IC_{50}) of these candidate metabolites. Half maximal inhibitory concentrations of these metabolites (f). The viral loads in the cell supernatant were detected with a plaque-formation assay at 40 h post-infection. The gray dotted line represents the 50% inhibition ratio ($n=3$ biological independent samples). Biological characterizations of candidate metabolic component(s) (g). Data are presented as the mean \pm s.e.m. (b,e,f). Data were analyzed using a two-tailed Student's *t*-test. *P* values were adjusted using Dunnett's test. *** $P<0.001$, **** $P<0.0001$. Experiments were performed independently at least three biological replicates with comparable results.

The fusion of the SARS-CoV-2 envelope with the host cell membrane is an essential process for viral entry³³. During viral entry, the binding of the receptor binding domain of the spike (S) protein to hACE2 (ref. ³⁴) promotes S1 subunits dissociation from the trimeric spike protein, thereby resulting in the extension of S2

subunits. Subsequently, the fusion peptides are inserted into the host cell membrane. The heptad repeat 1 (HR1) and 2 (HR2) domains in the S2 subunit of the S protein bind each other and form a six-helix bundle (6-HB) fusion core, which promotes the membrane fusion between viruses and host cells³⁵. We next exploited a SARS-CoV-2 S



protein-mediated cell–cell fusion assay to assess the role of 1,5-AG during SARS-CoV-2 membrane fusion. The 293T cells that express the SARS-CoV-2 S protein were used as effector cells; 293T/hACE2 cells expressing human ACE2 protein were exploited as target cells. The effector cells aggregated around the target cell to form a typical syncytium³⁵. Incubation with 1,5-AG inhibited the formation of syncytium between the effector cells and the target cells (Fig. 3d–f).

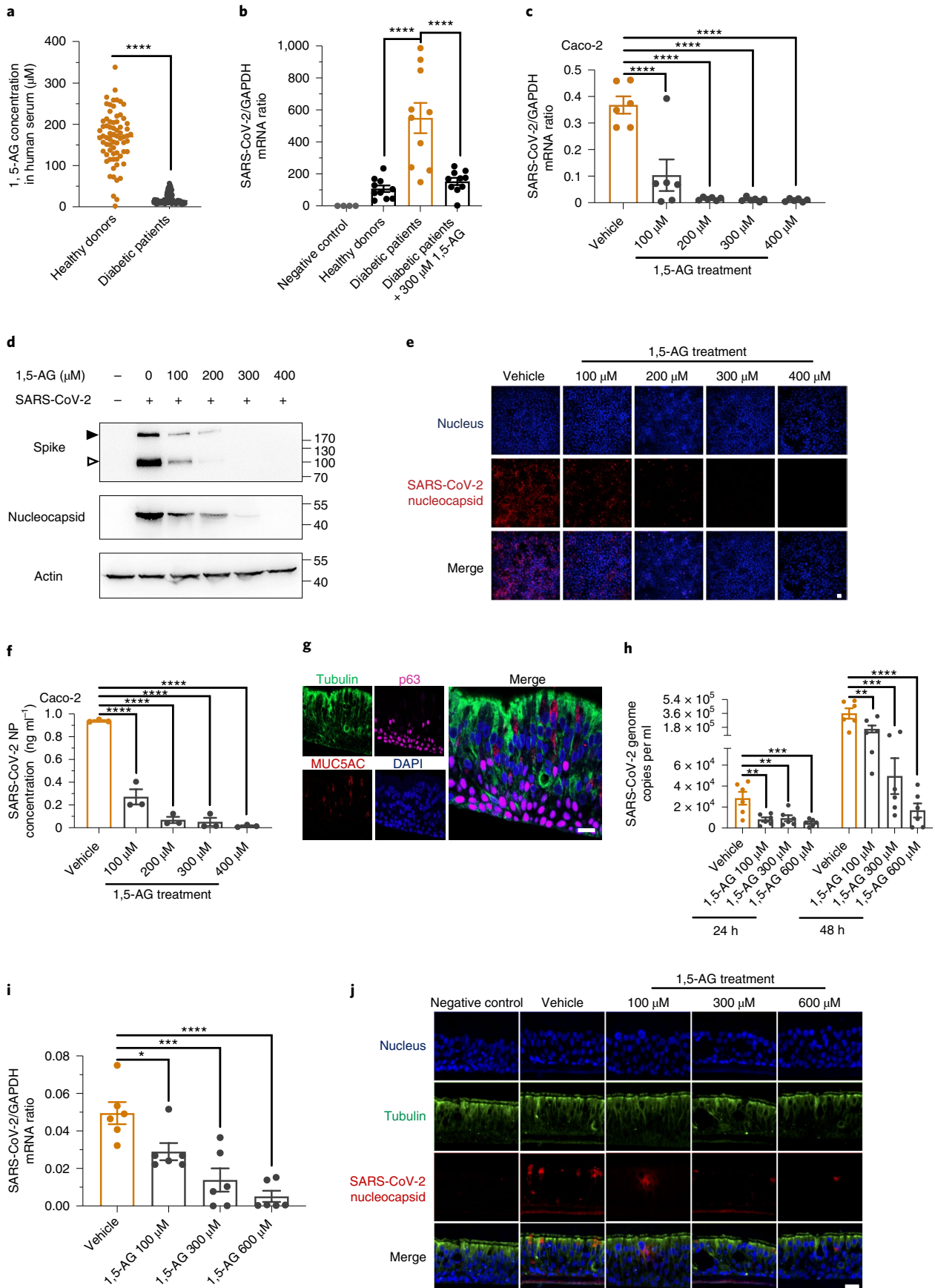
Virion fusion with target cells requires appropriate membrane fluidity for higher-affinity binding and lipid rearrangement. A reduction in membrane fluidity leads to the inhibition of virion entry³⁶. However, incubating with 1,5-AG did not influence membrane fluidity (Extended Data Fig. 2g,h). We next speculated that it may directly interact with the spike protein. According to the docking modeling, 1,5-AG does not directly associate with the trimeric spike protein of SARS-CoV-2. Nonetheless, the model suggested that 1,5-AG may bind to the V952 and N955 sites in the HR1 domain of the S2 subunit. This prediction was validated by surface plasmon resonance (SPR) with either the full-length spike (Fig. 3g) or the trimeric S2 subunit protein (Fig. 3h). Substituting both valine (V) to alanine (A) and asparagine (N) to alanine (A) at the two sites (named S2M) substantially reduced the binding affinity of 1,5-AG for the trimeric S2 protein (Fig. 3i and Extended Data Fig. 2i,j). Incubating with 1,5-AG largely impaired the formation of the 6-HB fusion core through the interaction of the HR1 and HR2 domains in a dose-dependent manner (Fig. 3j). We therefore conclude that 1,5-AG inhibits SARS-CoV-2 infection by directly binding to the S2 subunit, thereby interrupting S2-mediated membrane fusion.

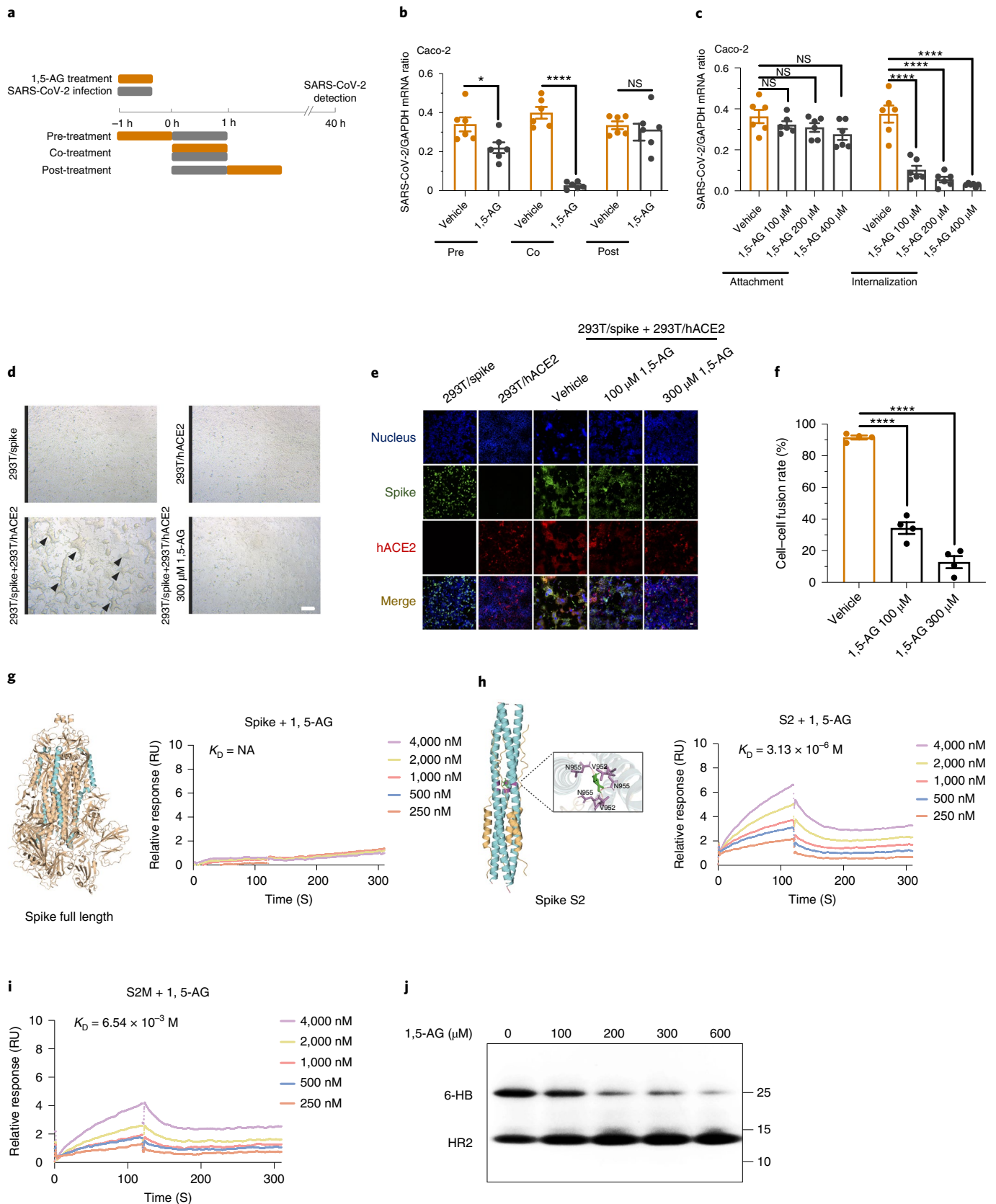
We next assessed whether 1,5-AG was still active against various emerging SARS-CoV-2 variants^{37,38}. A sequence comparison indicated that both of V952 and N955 in the spike protein are stable in all SARS-CoV-2 variants of concern (Extended Data Fig. 3a). A spike protein-pseudotyped human immunodeficiency virus system (HIV-CoV-2-S) was exploited to assess the role of 1,5-AG in inhibiting the cellular entry of these variants³⁵. Notably, 1,5-AG dose-dependently reduced the luciferase activity in both 293T/hACE2 and Caco-2 cells infected with these HIV-CoV-2-S variants (Extended Data Fig. 3b,c). Both V952 and N955 in the SARS-CoV-2 spike protein are also conserved in SARS-CoV and MERS-CoV (Extended Data Fig. 3d). 1,5-AG administration impaired the entry of the HIV-SARS-CoV-S pseudovirus into 293T/hACE2 cells, while reducing the invasion of HIV-MERS-CoV-S into Huh7 cells³⁵ (Extended Data Fig. 3e). Nonetheless, incubation with 1,5-AG did not influence the infection of these respiratory viruses such as the influenza A virus (IAV) H1N1 PR8 and WSN strains in a human pulmonary epithelium A549 cells and respiratory syncytial virus (RSV) in Vero cells (Extended Data Fig. 3f–h), suggesting the potential of 1,5-AG in the specific resistance of human coronaviruses.

We speculated that an 1,5-AG deficiency may contribute to SARS-CoV-2 pathogenesis in patients with diabetes. To address this, we exploited a db/db mouse model derived from C57BL/KsJ mice, which are currently the widely used mouse model of type 2 diabetes mellitus^{39,40}. The 1,5-AG concentration in serum^{41,42} and BALF of db/db mice was significantly lower than that in the C57BL/KsJ control mice (Fig. 4a and Extended Data Fig. 4a). First, we assessed the feasibility of 1,5-AG supplementation against SARS-CoV-2 infection in animals by intravenous administration. The peak concentration of 1,5-AG appeared at 1 h after administration and then rapidly decreased in the serum (Extended Data Fig. 4b); however, it remained the same in the lungs throughout the assessment (Extended Data Fig. 4c). We next delivered 1,5-AG into the mouse trachea by intratracheal administration⁴³. The abundance of 1,5-AG rapidly decreased to the physiological level in the lung within 3 h (Extended Data Fig. 4d), whereas there was no significant change in the serum (Extended Data Fig. 4e). These results indicated that either intravenous or intratracheal administration was not a feasible approach to manipulate the 1,5-AG abundance in mice. We therefore used a subcutaneous micro-osmotic pump with a sustained-releasing capacity to assess the role of 1,5-AG in SARS-CoV-2 infection in animals. Drug complementation in a sustained-releasing manner significantly enhanced the concentration of 1,5-AG in the mouse serum (Fig. 4a), lung (Fig. 4b) and BALF (Extended Data Fig. 4a).

Ten days after pump implantation, both 1,5-AG- and PBS-treated mice were infected with a mouse-adapted SARS-CoV-2 strain⁴⁴. The SARS-CoV-2 infection led to a decrease of 1,5-AG levels in the C57BL/KsJ and db/db mouse serum and lung (Extended Data Fig. 5a,b). We found that the body masses of both control PBS (C57BL/KsJ) and db/db 1,5-AG mice increased within 2 d after infection, then dropped to their basal level (day 0) at 3 d after infection and remained steady thereafter; however, the body masses of db/db PBS mice continued to drop significantly throughout 7 d of infection (Fig. 4c). Consistently, the db/db PBS mice had much higher SARS-CoV-2 loads in the lung, trachea and nasal turbinate, as detected by a 50% tissue culture infectious dose (TCID₅₀) assay (Fig. 4d–f), quantitative PCR with reverse transcription (qRT-PCR) (Extended Data Fig. 5c–e) and an immunofluorescence staining (Fig. 4g) and presented more severe pathological damage in the lung than the other two groups (Fig. 4h and Extended Data Fig. 5f). Altogether, these results suggest that 1,5-AG deficiency accounts for severe SARS-CoV-2 pathogenesis in diabetic mice. Sustained supplementation of 1,5-AG to a healthy level in diabetic mice restored the SARS-CoV-2 loads and disease severity to a lower level in the nondiabetic mice. We next explored the clinical relevance between 1,5-AG levels and COVID-19 severity, according to

Fig. 2 | 1,5-AG is a diabetes-associated antiviral metabolite that inhibits SARS-CoV-2 infection. **a,b**, 1,5-AG is a diabetes-associated anti-SARS-CoV-2 metabolite. Concentrations of 1,5-AG in the serum of patients with diabetes and healthy donors (**a**). The horizontal line is the median value. The data were analyzed using a nonparametric two-sided Mann-Whitney *U*-test. Each dot represents one donor ($n = 70$ healthy donors, $n = 69$ patients with diabetes). Supplementation with 1,5-AG in diabetic serum impaired SARS-CoV-2 infection in Vero cells (**b**). Each dot represents one donor ($n = 10$ healthy donors, $n = 10$ patients with diabetes). **c–f**, Antiviral activity of 1,5-AG in Caco-2 cells. The amount of viral RNA was determined by qRT-PCR ($n = 6$ biologically independent samples) (**c**). The spike or nucleocapsid proteins in infected cells were detected by western blotting (**d**), immunofluorescence staining (**e**) and ELISA ($n = 3$ biologically independent samples) (**f**). The black and the white arrowhead indicate the full-length spike and the cleaved form (**d**). Representative of three confocal immunofluorescence images from three biological replicates are shown (**e**). Scale bars, 20 μm . **g–j**, Antiviral activity of 1,5-AG in bronchiolar epithelial cultures. Green, ciliated cells; purple, basal cells; red, goblet cells; blue, nucleus (**g**). DAPI, 4,6-diamidino-2-phenylindole. Representative of three immunofluorescence images from three biological replicates are shown. Scale bars, 15 μm . Secreted viruses of infected bronchiolar epithelial cultures (**h**). $P = 0.002$ and $P = 0.0073$ for vehicle versus 1,5-AG 100 μM for 24 h and 48 h. $P = 0.0034$ and $P = 0.0001$ for vehicle versus 1,5-AG 300 μM for 24 h and 48 h. $P = 0.0005$ and $P < 0.0001$ for vehicle versus 1,5-AG 600 μM for 24 h and 48 h. The amount of viral RNA in bronchiolar epithelial cultures (**i**). $P = 0.0257$ for vehicle versus 1,5-AG 100 μM , $P = 0.0002$ for vehicle versus 1,5-AG 300 μM , $P < 0.0001$ for vehicle versus 1,5-AG 600 μM . Representative of three confocal immunofluorescence images from three biological replicates are shown (**j**). Scale bars, 20 μm . Each dot represents a bronchiolar epithelial culture ($n = 6$ bronchiolar epithelial cultures per group pooled from three independent biological replicates) (**h–j**). Data are mean \pm s.e.m. (**b–j**). Data were analyzed using a two-tailed Student's *t*-test. *P* values were adjusted using Dunnett's test. * $P < 0.05$; ** $P < 0.01$; *** $P < 0.001$ and **** $P < 0.0001$. Experiments were performed independently with at least three biological replicates with comparable results.





the available metabolomics data from patients with nonsevere and severe COVID-19 (refs. ^{10,45,46}) (Supplementary Table 3). The serum 1,5-AG levels in patients with COVID-19 with severe clinical manifestations, rather than in patients with nonsevere COVID-19, were significantly lower than those of the healthy participants (Fig. 4i),

thereby suggesting the association of 1,5-AG deficiency with severe SARS-CoV-2 infection.

Accumulating evidence has shown that endogenous metabolites in human blood may regulate host susceptibility or resilience to a viral infection^{47–54}. 1,5-AG, a glucose-like pyranoid polyol in

Fig. 3 | 1,5-AG inhibits SARS-CoV-2 infection by directly binding to the S2 subunit to interrupt membrane fusion. **a–c**, 1,5-AG inhibited SARS-CoV-2 internalization into human cells. Schematic diagram of the study design (**a**). Coincubation of 1,5-AG with the viruses suppressed SARS-CoV-2 infection (**b**). $P=0.0252$ and $P<0.0001$ for vehicle versus 1,5-AG of pre and co. 1,5-AG affected viral internalization but not attachment (**c**). Viral loads were determined at 40 h after infection by qRT-PCR ($n=6$ biological independent samples) (**b,c**). **d–f**, 1,5-AG interrupted spike-ACE2-mediated cell–cell membrane fusion. The capacity of cell–cell fusion was measured by microscopy (**d**) and immunofluorescence staining (**e**). The effector cells aggregated with the target cells to form typical syncytia (black triangle) (**d**). Scale bars, 200 μm . The spike protein was stained with Alexa Fluor 488-conjugated anti-mouse IgG (**e**). Human ACE2 protein was stained with Alexa Fluor 546-conjugated anti-rabbit IgG. The nuclei were stained with To-Pro-3 iodide. Representative of four confocal immunofluorescence images from four biological replicates was shown. Scale bars, 20 μm . The confocal microscope of fused and unfused cells were counted by ImageJ (**f**). **g–i**, 1,5-AG interacted with the S2 subunit to interrupt the formation of 6-HB. 1,5-AG did not associate with the trimeric spike protein of SARS-CoV-2 (**g**). 1,5-AG is directly associated with the S2 subunit of the spike protein (**h**). Prediction of the association between 1,5-AG and spike/S2 protein (**g,h**, left). Interaction between 1,5-AG and spike/S2 protein detected by SPR (**g,h**, right). The substitution of both V and N to A at site 952 and 955 in the HRI domain substantially reduced the binding affinity of 1,5-AG for the S2 protein (**i**). The binding affinity of 1,5-AG and S2M was measured by SPR. RU, relative unit. **j**, 1,5-AG impaired the interaction of HRI and HR2 to inhibit 6-HB formation. The capacity of 6-HB formation was detected by nondenaturing electrophoresis. Data are mean \pm s.e.m. (**b,c,f**). The data were analyzed using a two-tailed Student's *t*-test. *P* values were adjusted using Dunnett's test to account for multiple comparisons. * $P<0.05$; **** $P<0.0001$; NS, not significant. Experiments were performed independently with at least three biological replicates with comparable results (**b–j**).

the human body, presents an effective anti-SARS-CoV-2 activity by binding to the S2 subunit of the SARS-CoV-2 spike protein, thereby interrupting spike-mediated virus–host membrane fusion. 1,5-AG is a short-term marker of glycemic control and serum levels of 1,5-AG are significantly lower in patients with diabetes than the healthy individuals¹¹. Our results suggest that a low level of 1,5-AG in diabetic people might, in part, underlie a high risk for severe COVID-19, therefore revealing the importance of 1,5-AG-mediated metabolic homeostasis in COVID-19 pathogenesis and suggesting that 1,5-AG supplementation and amelioration of hyperglycemia in patients with diabetes might help to reduce the incidence and/or prevent severe COVID-19.

Methods

Ethics statement. Human blood samples were collected with approval of the local ethics committee at Tsinghua University and Shenzhen Centers for Disease Control and Prevention. Human blood collected from healthy donors who provided written informed consent was used for the experiments. Human airway biopsies were collected with written informed consent from pulmonary bulla patients with approval of the local ethics committee at Shenzhen Institutes of Advanced Technology, Chinese Academy of Sciences and No.7 Affiliated Hospital of Zhongshan University. All animal experiments involving infectious virus were conducted in Biosafety Level 3 laboratory (BSL-3) and approved by the Animal Experiment Committee of Laboratory Animal Center, Beijing Institute of Microbiology and Epidemiology (approval no. IACUC-IME-2021-017).

Mice. All animal protocols used in this study were approved by the Institutional Animal Care and Use Committee of Tsinghua University and performed in accordance with their guidelines. The laboratory animal facility has been accredited by the Association for Assessment and Accreditation of Laboratory Animal Care International. Six-week-old BKS-leprdb (db/db, C57BL/KsJ background) and C57BL/KsJ control mice were purchased from GemPharmatech Co. Six-week-old C57BL/6J mice were purchased from Charles River. All animals were maintained in a specific pathogen-free animal facility at Tsinghua University with a 12-h light/dark cycle and normal chow diet and water.

Cell lines, viruses, plasmids and peptides. The 293T, Vero, Caco-2, A549, MDCK, HepG2 cells were obtained from the American Type Culture Collection (cat. no. CRL3216, CCL81, HTB37, CCL-185, CCL-34 and HB-8065). Huh7 cells were obtained from JCRB (cat. no. JCRB0403). The 293T cells expressing human ACE2 (293T/hACE2) were kindly provided by Q. Ding from Tsinghua University. All cell lines were maintained in Dulbecco's modified Eagle's medium (DMEM) (Gibco, cat. no. 11965-092) supplemented with 10% heat-inactivated fetal bovine serum (FBS) (Gibco, cat. no. 16000-044) and 1% antibiotic-antimycotic (Gibco, cat. no. 15240-062) at 37°C and 5% CO₂. SARS-CoV-2 (GISAID accession number, EPI_ISL_413879) was passaged in Vero cells cultured in DMEM supplemented with 2% FBS. Influenza A virus (IAV) H1N1 (A/PR/8/34 strain and A/WSN/33 strain) was passaged in MDCK cells cultured in DMEM supplemented with 0.5 mg ml⁻¹ *N*-p-tosyl-phenylalanine chloromethyl ketone (TPCK)-treated trypsin (Sigma, cat. no. T1426) and 0.3% FBS. RSV A strain was passaged in HepG2 cells cultured in DMEM supplemented with 2% FBS. The SARS-CoV-2, H1N1 (PR8 strain and WSN strain) and RSV A strain titer were determined by a plaque-formation assay. Cells were cultured in DMEM supplemented with 2% FBS in the cell infection experiments. Mouse-adapted SARS-CoV-2 strain (MASCp36)⁴⁴ was kindly provided by C. Qin from State Key Laboratory of Pathogen and Biosecurity. The virus stock of MASCp36 was titrated by standard plaque-forming assay on Vero cells. The HRI (ANQFNSAIGKIQDSLSTASALGKQLQDVVNQNAQALNTLVKQ) and HR2 (DISGINASVNVNIQKEIDRLNEVAKNLSLIDLQEL) peptides of the spike S2 region were synthesized by China Peptides Co. Plasmids expressing the SARS-CoV-2 wild-type spike protein (pcDNA3.1-SARS-2-S) were kindly provided by L. Lu from Fudan University. Plasmids expressing the spike proteins of SARS-CoV-2 variants pcDNA3.1-B.1.1.7-S, pcDNA3.1-P.1 (501Y.V3)-S, pcDNA3.1-B.1.351 (20HY)-S, pcDNA3.1-B.1.351-V1-S, pcDNA3.1-B.1.351-V2-S, pcDNA3.1-B.1.351-V3-S, pcDNA3.1-B.1.617-S, pcDNA3.1-B.1.1.529-S and pNL4-3.luc.RE (the luciferase reporter-expressing HIV-1 backbone) were maintained in our laboratory. Plasmids expressing the spike protein of SARS-CoV (pcDNA3.1-SARS-CoV-S) and MERS-CoV (pcDNA3.1-MERS-CoV-S) were kindly provided by L. Zhang from Tsinghua University.

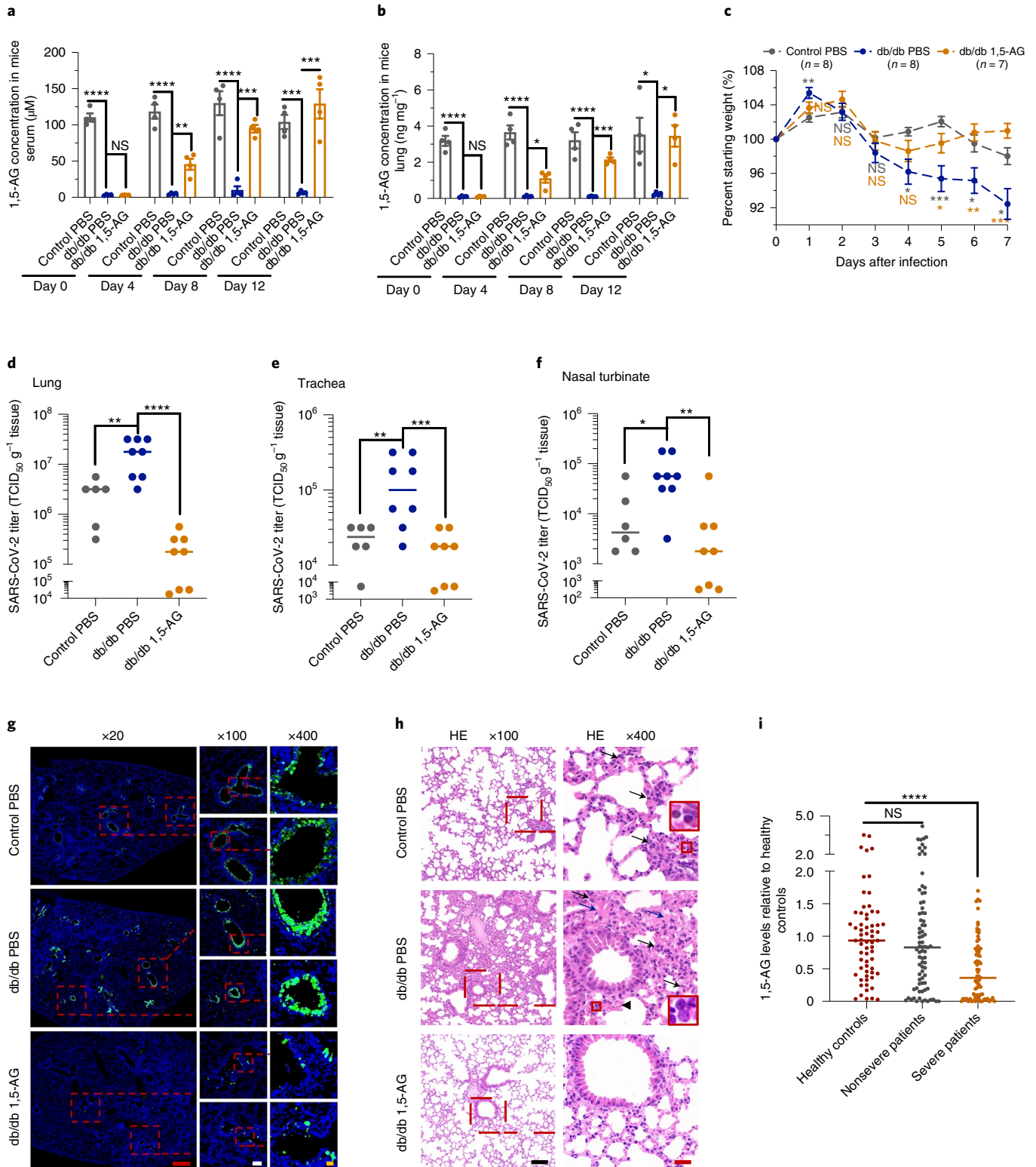
Analysis of human serum metabolic components by LC–MS/MS. The nontargeted metabolomic profiles of serum samples collected from three individuals were measured by liquid chromatography–tandem mass spectrometry (LC–MS/MS) at the Tsinghua Metabolic Center to analyze metabolic components in human serum. Blood samples collected from three healthy donors were

Fig. 4 | Restoration of 1,5-AG reduced SARS-CoV-2 infection and prevented the lung pathology in db/db mice. **a,b**, Metabolic kinetics of 1,5-AG in serum (**a**) and lung (**b**) of mice implanted with osmotic pumps ($n=4$ mice). $P=0.001$ and $P=0.0102$ for control PBS versus db/db PBS at day 12 of serum and lung. $P=0.0056$, $P=0.0006$ and $P=0.0002$ for db/db PBS versus db/db 1,5-AG at day 4, 8 and 12 of serum. $P=0.0472$, $P=0.001$ and $P=0.0114$ for db/db PBS versus db/db 1,5-AG at day 4, 8 and 12 of lung. **** $P<0.0001$. **c**, The weight change of infected mice. Gray *P* values, control PBS versus db/db PBS. Orange *P* values, db/db PBS versus db/db 1,5-AG. $P=0.0057$, $P=0.0140$, $P=0.0009$, $P=0.0320$ and $P=0.0111$ for control PBS versus db/db PBS at day 1, 4, 5, 6 and 7. $P=0.0374$, $P=0.0076$ and $P=0.0004$ for db/db PBS versus db/db 1,5-AG at day 5, 6 and 7. **d–f**, SARS-CoV-2 loads in the lung (**d**), trachea (**e**) and nasal turbinate (**f**) of infected mice. Each dot represents one mouse ($n=6$ control PBS, $n=8$ db/db PBS and $n=8$ db/db 1,5-AG, male:female, 1:1). $P=0.0073$, $P=0.0096$ and $P=0.0432$ for control PBS versus db/db PBS of lung, trachea and nasal turbinate. $P<0.0001$, $P=0.0006$ and $P=0.0011$ for db/db PBS versus db/db 1,5-AG of lung, trachea and nasal turbinate. **g**, Immunofluorescence staining of lungs. A representative of three images from three biological replicates is shown. Scale bars, 500 μm (red), 100 μm (white) and 20 μm (orange). **h**, Histopathology of lungs. Red frame, lymphocyte infiltration; triangle, interstitial congestion; blue frame, protein accumulation. A representative of three images from three biological replicates is shown. Scale bars, 100 μm (black), 10 μm (red). **i**, Reduction of serum 1,5-AG is associated with clinical COVID-19 severity. One dot represents one patient ($n=64$ healthy controls, $n=79$ nonsevere patients and $n=71$ severe patients). Data were analyzed using a nonparametric two-sided Mann–Whitney *U*-test and adjusted using a Dunnett's test (**a–f,i**). * $P<0.05$; ** $P<0.01$; *** $P<0.001$; and **** $P<0.0001$. Data are mean \pm s.e.m. (**a–c**). The horizontal line is the median value (**d–f,i**). Experiments were performed independently at least three biological replicates with comparable results (**c–h**).

extracted with cold methanol, mixed and incubated at -80°C overnight. The supernatant was separated by centrifugation at $14,000g$ for 10 min at 4°C and dried to produce a pellet by a SpeedVac. The dried samples were sent for LC-MS/MS analysis. Briefly, an Ultimate 3000 UHPLC (Dionex) coupled with an Orbitrap mass spectrometer (Thermo Fisher) was used to perform LC separation. In negative mode, a BEH C18 column (Waters, cat. no. 186002352) was applied for analysis at a flow rate of 0.25 ml min^{-1} . Spectra with mass ranges of m/z 80–1,200 and m/z 70–1,050 were acquired in positive ion mode and negative ion mode with data-dependent MS acquisition. TraceFinder 3.2 (Thermo Scientific) was used for metabolite identification with an in-house library containing MS/MS spectra from

over 1,500 metabolites. Mass tolerances of 10 ppm and 15 ppm were applied for the precursor and fragment searches. Metabolites were assigned based on fragment matching with MS/MS spectra in the library.

Serum levels of 1,5-AG, 5-MT and CDCA were quantitatively analyzed by LC-MS/MS. The sample extraction procedure was the same as described above. Fifty nanograms of D5-tryptophan (JK Scientific, cat. no. T947207), 50 ng of D9-CDCA (Isoscience, cat. no. 13103) and 50 ng of 1,5-AG- $^{13}\text{C}_6$ (Omicron, cat. no. ALD069) were used as internal standards. Data were acquired in multiple reaction monitor (MRM) mode for 1,5-AG in negative ion mode with transitions of 162.8/100.8. The ion transitions were optimized using chemical standards.



The nebulizer gas (Gas1), heater gas (Gas2) and curtain gas were set at 55, 55 and 30 psi, respectively. The ion spray voltage was $-4,500$ V for negative ion mode. The optimal probe temperature was determined to be 500°C and the column oven temperature was set to 45°C . Data were MRM mode for 5-MT with transitions of 142.9/115 in negative ion mode. CDCA analysis was performed using Q Exactive HFX Orbitrap (Thermo Scientific).

Anti-SARS-CoV-2 serum metabolites screening. All 222 compounds were dissolved in dimethyl sulfoxide (DMSO) and diluted with cell culture medium. Vero cells were preincubated with a $100\ \mu\text{M}$ solution of each compound at 37°C for 1 h and then infected with 0.001 multiplicity of infection (MOI) SARS-CoV-2 for 1 h. Cells were washed and cultured with medium containing $100\ \mu\text{M}$ compounds for an additional 40 h to detect the viral burden by qRT-PCR. Information on these compounds is listed in Supplementary Table 2.

The roles of human serum in SARS-CoV-2 infection. Human serum samples were separated by centrifugation with a 3 kDa filter (Millipore, cat. no. UFC900396). Either the filtrates containing small-molecule metabolites or the upper retentate with serum proteins were diluted twofold with cell medium, incubated with Vero cells at 37°C for 1 h. Cells were then infected with 0.001 MOI SARS-CoV-2 for 40 h and collected to detect the viral burden using qRT-PCR. Vero cells incubated with cell medium with or without SARS-CoV-2 infection served as infected or uninfected controls.

Human serum from healthy individuals and patients with diabetes was collected to assess their role in SARS-CoV-2 infection. The serum was diluted twofold with DMEM, incubated with Vero cells at 37°C for 1 h. Cells were then infected with 0.001 MOI SARS-CoV-2 for 24 h and collected to detect the viral burden using qRT-PCR.

Detection of the viral burden by qRT-PCR. Total RNA was isolated from infected cells using a Multisource RNA Miniprep kit (Axygen, cat. no. AP-MN-MS-RNA-250) and reverse transcribed to complementary DNAs using an iScript cDNA Synthesis kit (Bio-Rad, cat. no. 1708890). The viral genomes were quantified with qRT-PCR using iTaq Universal SYBR Green Supermix (Bio-Rad, cat. no. 1725121). qRT-PCR was performed using a Bio-Rad CFX-96 Touch Real-Time Detection System. The primer sequences are shown in Supplementary Table 4. The amount of virus was normalized to human *GAPDH* (GenBank, no. NC_000012.12) or mouse *GAPDH* (GeneBank, no. NC_000072.7).

Cytotoxicity assay. The cytotoxicity of the metabolites toward the cells was measured by Cell Counting Kit-8 (CCK-8) (Meilunbio, cat. no. MA0218-1) assay. Vero cells were pre-seeded in a 96-well plate (10^4 cells per well). Cells were treated with gradient concentrations of the compounds at 37°C for 48 h. The CCK-8 solution ($10\ \mu\text{l}$ per well) was added, incubated at 37°C for 1 h. The absorbance was measured at 450 nm. The concentration of each compound necessary to reduce cell viability by 50% (CC_{50}) was calculated by comparing the values with DMSO-treated cells using a sigmoidal nonlinear regression function in GraphPad Prism 8.0 (GraphPad Software) to fit the dose-response curve.

IC_{50} quantification. Vero cells were pre-seeded in a 48-well plate (2×10^4 cells per well). Nine-point dose-response curves were generated with compound concentrations ranging from 3.125 to $400\ \mu\text{M}$. Cells were preincubated with the compounds at 37°C for 1 h and then infected with 0.001 MOI SARS-CoV-2 for 1 h. The cells were then washed and cultured with fresh medium containing the compound for 40 h. The supernatant was collected to determine the viral titer by a plaque-formation assay. The concentration of each compound required to inhibit viral infection by 50% (IC_{50}) was calculated by comparing the values with the DMSO-treated cells in GraphPad Prism 8.0 (GraphPad Software).

Western blot analysis. Caco-2 cells were preincubated with 1,5-AG at 37°C for 1 h. Cells were infected with SARS-CoV-2 at 0.01 MOI for 1 h, washed and then cultured in DMEM containing 1,5-AG for 40 h. Cells were collected in $300\ \mu\text{l}$ of lysis buffer supplemented with a protease inhibitor cocktail (Thermo Scientific, cat. no. 1862209). The lysates were centrifuged and denatured at 100°C for 10 min for western blot analysis. The following antibodies were used: anti-SARS-CoV-2 spike (Abcam, cat. no. ab273433), anti-SARS-CoV-2 nucleocapsid (Abcam, cat. no. ab271180) and anti-actin (Cell Signaling Technology, cat. no. 3700).

Immunofluorescence staining and microscopy. Cells were washed and fixed with 4% paraformaldehyde (PFA) for 2 h. Then, the cells were permeabilized with 0.1% Triton X-100 for 30 min, washed and blocked with 2% BSA for 1 h. The cells were stained with anti-SARS-CoV-2 nucleocapsid (Abcam, cat. no. ab271180), anti-SARS-CoV-2 spike (Abcam, cat. no. ab273433) and anti-hACE2 (Abcam, cat. no. ab108252) antibodies for 2 h at room temperature, according to different experimental settings. The cells were washed and then stained with fluorescent dye-conjugated secondary antibodies for 1 h at room temperature. The nuclei were stained with To-Pro-3 iodide (Invitrogen, cat. no. T3605). Images were captured using a Zeiss LSM 880 meta confocal microscope.

Air-liquid interface epithelial cultures and viral infection. ALI human epithelial cultures at day 28 were utilized to evaluate antiviral activity. 1,5-AG was diluted and added to a single epithelium-containing Transwell in a 24-well plate and incubated at 37°C for 30 min. Then, 1,000 plaque-forming units (p.f.u.) of SARS-CoV-2 was added, followed by incubation at 37°C for 1 h. The inoculum was removed and washed three times to remove unbound virus and 1,5-AG was added to the Transwell for further incubation. At 24 h and 48 h after infection, $150\ \mu\text{l}$ of PBS were added to the top surface of each epithelial culture and then collected for analysis. Viral genome copies in the collected samples were then determined using qRT-PCR. At 48 h after infection, the epithelia were collected for virus burden quantification.

Multiplex immunofluorescence staining of ALI cultures. ALI cultures were embedded in paraffin and sectioned at a thickness of $3\ \mu\text{m}$ for multiplex immunofluorescence staining. The paraffin sections were deparaffinized in xylene and rehydrated in a graded series of alcohol solutions, followed by an incubation in citrate buffer (pH 6.0) with microwaving at 95°C for 20 min for antigen retrieval. Multiplex fluorescence labeling was exploited using TSA-dendron-fluorophores with a NEON 7-color Allround Discovery kit for FFPE (Histova Biotechnology, cat. no. NEFP750). Briefly, endogenous peroxidases were quenched with 3% H_2O_2 for 20 min and then blocked for 30 min. The ALI cultures were stained with the primary antibody for 2 h, followed by detection using an HRP-conjugated secondary antibody and TSA-dendron-fluorophores. Afterwards, the primary and secondary antibodies were thoroughly eliminated by incubating the sections in retrieval/elution buffer for 10 s at 95°C . Each antigen was labeled with different fluorophores. The following antibodies were used: β -IV-tubulin (Abcam, cat. no. ab179504), MUC5AC (Abcam, cat. no. ab198294), p63 (Abcam, cat. no. ab53039) and anti-SARS-CoV-2 spike (Abcam, cat. no. ab273433). After all the antibodies were detected sequentially, the epithelial sections were stained with DAPI (Abcam, cat. no. ab228549) and cleared with the clearing-enhanced 3D method. Images were captured by a Zeiss LSM 880 meta confocal microscope.

Inhibition of pseudotyped coronavirus infection. The 293T cells were co-transfected with the pNL4-3.luc.RE backbone and pcDNA3.1-SARS-2-S, pcDNA3.1-B.1.1.7-S, pcDNA3.1-P1 (501Y.V3)-S, pcDNA3.1-B.1.351 (20HY)-S, pcDNA3.1-B.1.351-V1-S, pcDNA3.1-B.1.351-V2-S, pcDNA3.1-B.1.351-V3-S, pcDNA3.1-B.1.617-S, pcDNA3.1-B.1.1.529-S, pcDNA3.1-SARS-CoV-S or pcDNA3.1-MERS-CoV-S plasmid. The supernatant was collected at 48 h post-transfection. The 293T/hACE2, Caco-2 or Huh7 cells were pre-seeded in a 96-well plate (10^4 cells per well). Pseudovirus was mixed with gradient concentrations of 1,5-AG at 37°C for 1 h. The mixture was then transferred to the cells. The medium was changed after 12 h and incubated for another 24 h. Cells were washed and then lysed with passive lysis buffer (Promega, cat. no. E1941). Luciferase activity was analyzed using a Luciferase Assay System (Promega, cat. no. E1910).

Surgical procedures and 1,5-AG administration. The 6-week-old C57BL/KsJ and db/db mice were anesthetized with 0.75% pentobarbital sodium and then implanted with an ALZet Model 2002 micro-osmotic pump (Charles River) releasing either PBS or 1,5-AG (2.5 M in PBS). Mice serum, lung and BALF were collected at indicated time points after the surgeries for 1,5-AG quantification. Mice were intranasally infected with 8,000 p.f.u. of MASCp36 at 10 d following the surgeries. Body weight was monitored daily. At 3 d after infection, a subset of mice was killed and tissue samples were collected for qRT-PCR, TCID_{50} (ref. ³⁵), histopathology and immunofluorescence analysis.

For the injection assay, 6-week-old male C57BL/6J mice were intravenously injected with $125\ \mu\text{l}$ of 10 mM 1,5-AG through the tail vein. For the intratracheal administration assay, a total of $50\ \mu\text{l}$ of 10 mM 1,5-AG was aerosolized into mice using the MicroSprayer Aerosolizer³³. The serum and lung tissue were collected at the indicated time points for 1,5-AG quantification.

Histological analysis and antigen staining. Lungs were collected, fixed and then embedded in paraffin and sectioned at a thickness of $3\ \mu\text{m}$. Sections were stained with hematoxylin and eosin to identify the histopathological changes. The sections were stained with anti-SARS-CoV-2 (Abcam, cat. no. ab271180) nucleocapsid antibodies for 2 h, washed and then stained with fluorescent dye-conjugated secondary antibodies for 1 h at room temperature. The nuclei were stained with DAPI (Abcam, cat. no. ab228549). Images were captured using a Zeiss LSM 880 meta confocal microscope.

A semiquantitative assessment was performed as reported³⁶. Three random fields of one tissue at $\times 400$ total magnification were chosen and scored in a blinded manner for the acute lung injury histological scoring system. The following parameters were analyzed: (A) neutrophils in the alveolar space (none, 0; 1–5 cells, 1; >5 cells, 2); (B) neutrophils in the interstitial space/septae (none, 0; 1–5 cells, 1; >5 cells, 2); (C) hyaline membranes (none, 0; one membrane, 1; >1 membrane, 2); (D) proteinaceous debris in air spaces (none, 0; one instance, 1; >1 instance, 2); and (E) alveolar septal thickening ($>2 \times$ mock thickness, 0; $2-4 \times$ mock thickness, 1; $>4 \times$ mock thickness, 2). The scores were calculated as follows: $((20 \times A) + (14 \times B) + (7 \times C) + (7 \times D) + (2 \times E)) / 100$. The final scores were obtained by averaging three fields per mouse.

Time course inhibition assay. Caco-2 cells were grown in 48-well plates and infected with 0.01 MOI for 1 h at 37°C to estimate the effect of 1,5-AG on the SARS-CoV-2 replication cycle. 1,5-AG was added 1 h before (Pre), simultaneously with (Co) or 1 h after (Post) SARS-CoV-2 inoculation. For the pre-treatment assay, cells were incubated with 1,5-AG for 1 h at 37°C, washed and infected with SARS-CoV-2 for 1 h. For the co-treatment assay, cells were simultaneously incubated with SARS-CoV-2 and 1,5-AG. After 1 h, the mixture was removed and the cells were washed before fresh medium was added. For the post-treatment assay, cells were first infected with SARS-CoV-2 for 1 h, followed by three washes and then incubated with medium containing 1,5-AG for 1 h. Then, the cells were washed and cultured with fresh medium for 40 h. Caco-2 cells were collected and the amount of viral RNA was detected by qRT-PCR.

A time of addition assay was performed to determine the specific stage of the viral entry process affected by 1,5-AG. For the attachment assay, Caco-2 cells were pre-cooled on ice and then incubated with a mixture of 1,5-AG and SARS-CoV-2 for 1 h at 4°C. Then, the cells were washed with pre-cooled PBS to remove the unbound viruses and incubated at 37°C for 40 h for viral burden detection. For the internalization assay, Caco-2 cells were pre-cooled on ice and then infected with SARS-CoV-2 at 4°C for 1 h. Afterwards, the cells were washed and incubated with medium containing 1,5-AG at 37°C for 1 h. Then, the cells were washed and cultured in fresh medium for 40 h for viral burden detection.

Inhibition of cell–cell fusion. The 293T cells expressing the SARS-CoV-2 spike protein (4×10^5 cells per well) and 293T cells expressing human ACE2 protein (1×10^5 cells per well) were mixed and incubated in the absence or presence of 1,5-AG at the indicated graded concentrations at 37°C for 1 h. Then, the cells were seeded in a 24-well plate at 37°C for 24 h. The fused and unfused cells were counted under a confocal microscope. Four images stained with To-Pro-3 iodide were individually selected from four biological replicates and used for counting the fused and unfused cells. The fused cell was much larger by at least twofold than the unfused cell³⁵. The percent inhibition of cell–cell fusion was calculated using the following formula (number of fused cells / number of the fused and unfused cells) \times 100%.

Real-time glycolytic assays. A Seahorse XFe96 Extracellular Flux analyzer (Agilent) was used to determine the bioenergetic profile of Vero cells. Vero cells were plated in XFe96 plates at a density of 10^4 cells per well 12 h before the experiment; 1,5-AG was added 2 h after seeding the cells and was removed before the test. Glycolytic stress tests were performed using an XFe96 Bioanalyzer at 12 h after seeding and all assays were performed according to the manufacturer's protocols. Results were normalized to the cell number.

Molecular docking models between 1,5-AG, spike and S2. For the docking assay, the trimeric spike protein (PDB accession no. 6VXX) and heteroatom-removed S2 subunit (PDB accession no. 6LXT) structures were treated as rigid and 1,5-AG was flexible. The grid box ($126.0 \text{ \AA} \times 126.0 \text{ \AA} \times 126.0 \text{ \AA}$) centered at the center of 6VXX and ($47.3 \text{ \AA} \times 47.3 \text{ \AA} \times 47.3 \text{ \AA}$) centered at the center of 6LXT was used in the docking experiment. The Lamarckian genetic algorithm was utilized at 100 runs in the AutoDock4 tools⁵⁷. The threshold of the mean binding energy was determined to be $-4.0 \text{ kcal mol}^{-1}$.

Purification of spike S2 and S2M proteins of SARS-CoV-2. The SARS-CoV-2 S2 subunit expression plasmid was kindly provided by Y. Zhu from the Institute of Biophysics, Chinese Academy of Science. A SGGRGG linker was used to link the coding sequences of the HR1 (910–988) and HR2 (1162–1206) domains of SARS-CoV-2 S2 subunits³⁵. For the S2M sequence, both V952 and N955 were substituted with alanine. Then sequences were cloned into a pET-28a-SUMO-His vector and transformed into BL21 (DE3) strain. Protein expression was induced with 0.5 mM IPTG at 16°C overnight. The fusion proteins were purified with TALON metal affinity resin (Takara, cat. no. 635501) and treated with SUMO protease (Solarbio, cat. no. P2070). S2 and S2M proteins were concentrated and filtered on a 10/300 Superdex 75 (GE Healthcare, cat. no. 17-5174-01) column. Peak fractions containing the S2 or S2M trimer were pooled and concentrated through centrifugation (Millipore, cat. no. UFC910008). The purified full-length spike protein was kindly provided by Y. Xiang from Tsinghua University.

Surface plasmon resonance analysis. SPR experiments were performed using a Biacore 8K system at 25°C with a flow rate of $30 \mu\text{l min}^{-1}$ in 0.05% PBST (PBS supplemented with 0.05% Tween-20, pH 7.4). For the SPR measurement at pH 4.5, the purified proteins were coupled to a CM5 sensor chip (GE Healthcare, cat. no. BR100530) with approximately 8,000 response units and concentrations of 1,5-AG ranging from 250 to 4,000 nM flowed over the chip surface. The binding kinetics and affinity were analyzed using Biacore Insight Evaluation software (GE Healthcare).

Inhibition of 6-HB formation assay. Five micrograms of the HR1 peptide were incubated with 1,5-AG at room temperature for 30 min and 5 μg of the HR2 peptide were added and further incubated at room temperature for 3 h, allowing HR1–HR2 complex formation. The mixture was subsequently analyzed by nondenaturing electrophoresis on a 15% Tricine gel.

Fluorescence recovery after photobleaching in 293T cells. The 293T cells were treated with 1,5-AG for 1 h and then stained with $2 \mu\text{g ml}^{-1}$ BODIPY 500/510 C1 and C12 (Invitrogen, cat. no. D3823) for 10 min at 37°C⁵⁸. Fluorescence recovery after photobleaching images were acquired with an Olympus FV3000 confocal microscope equipped with a live cell chamber and Olympus FV31S-SW software (Olympus) with a $\times 65$ oil immersion objective. Cells were excited with a 488 nm laser and the emission was recorded between 493 and 589 nm. Images were acquired with 16-bit image depth and 512×512 resolution. Five pre-bleaching images were collected and then the region of interest was bleached with 17% laser power. The recovery of fluorescence was traced for 200 s. Fluorescence recovery and T_{half} were calculated by Olympus cellSens software (Olympus).

ELISA. The amount of nucleocapsid protein in the supernatant of Caco-2 cells was detected by the SARS-CoV-2 nucleocapsid detection ELISA kit (SinoBiological, cat. no. KIT40588). One hundred microliters of diluted standards or samples were added to the plate at room temperature for 2 h. After three washes, 100 μl of detection antibody (0.2 mg ml^{-1}) was added at room temperature for 1 h. The microplate was washed for four times, the substrate solution was added and incubated at room temperature for 20 min. The absorbance was determined at 450 nm.

The hACE2 precoated microplate from the SARS-CoV-2 Surrogate Virus Neutralization Test kit (GenScript, cat. no. L00847) was used in the ELISA. One microgram of SARS-CoV-2 spike protein with a streptavidin tag was incubated with 1,5-AG at 37°C for 1 h. PBS was used as a negative control and the hACE2 antibody was a positive control. The mixture was added to the precoated microplate at 37°C for 15 min and washed three times. HRP-labeled streptavidin (Beyotime, cat. no. A0303) was added at a dilution of 1:4,000 and incubated at 37°C for 45 min. After four washes, the substrate solution was added to the microplate and incubated at room temperature. The absorbance was detected at 450 nm.

1,5-AG abundance in healthy donors and patients with COVID-19. Data on the presence of 1,5-AG in the serum of both healthy participants and patients with COVID-19 were extracted from the available raw data of three metabolomic studies (Supplementary Table 3), in which a total of 64 healthy participants and 150 patients with COVID-19 (79 with nonsevere and 71 with severe clinical manifestations) were included. The clinical quantification of disease severity was based on the World Health Organization Ordinal Scale (WOS). The presence of serum 1,5-AG was normalized to the mean value of serum 1,5-AG in the healthy participants according to the available raw data. The nonsevere COVID-19 group included the patients with mild and moderate COVID-19 with a WOS score of 1–4, whereas the severe COVID-19 group included patients with severe, critical and fatal COVID-19 with a WOS score 5–8.

Statistics. Animals were randomly allocated into different groups. Descriptive statistics are provided in the figure legends. Analyses of independent data were performed using the two-tailed Student's *t*-test and nonparametric Mann–Whitney *U*-test, as appropriate. The *P* values were adjusted using Dunnett's test to account for multiple comparisons. Statistical analyses were carried out using GraphPad Prism 8.0. *P* values < 0.05 were considered significant. Significance values were set as follows: NS, not significant, $P > 0.05$; * $P < 0.05$; ** $P < 0.01$; *** $P < 0.001$; and **** $P < 0.0001$.

Reporting Summary. Further information on research design is available in the Nature Research Reporting Summary linked to this article.

Data availability

The numeric source data are provided in source data files. All data and materials that support the findings of this study are available from the corresponding author upon reasonable request. Source data are provided with this paper.

Received: 9 October 2021; Accepted: 29 March 2022;

Published online: 9 May 2022

References

- Mayer, K. A., Stöckl, J., Zlabinger, G. J. & Gualdoni, G. A. Hijacking the supplies: metabolism as a novel facet of virus–host interaction. *Front. Immunol.* **10**, 1533 (2019).
- La Torre, F. et al. Immunological basis of virus–host interaction in COVID-19. *Pediatr. Allergy Immunol.* **26**, 75–78 (2020).
- Hu, B., Guo, H., Zhou, P. & Shi, Z. L. Characteristics of SARS-CoV-2 and COVID-19. *Nat. Rev. Microbiol.* **19**, 141–154 (2021).
- Wang, C., Horby, P. W., Hayden, F. G. & Gao, G. F. A novel coronavirus outbreak of global health concern. *Lancet* **395**, 470–473 (2020).
- Williamson, E. J. et al. Factors associated with COVID-19-related death using OpenSAFELY. *Nature* **584**, 430–436 (2020).
- Clark, A. et al. Global, regional, and national estimates of the population at increased risk of severe COVID-19 due to underlying health conditions in 2020: a modelling study. *Lancet Glob. Health* **8**, 1003–1017 (2020).

7. Zhou, F. et al. Clinical course and risk factors for mortality of adult inpatients with COVID-19 in Wuhan, China: a retrospective cohort study. *Lancet* **395**, 1054–1062 (2020).
8. Bar, N. et al. A reference map of potential determinants for the human serum metabolome. *Nature* **588**, 135–140 (2020).
9. Ricklin, D., Hajishengallis, G., Yang, K. & Lambris, J. D. Complement: a key system for immune surveillance and homeostasis. *Nat. Immunol.* **11**, 785–797 (2010).
10. Wu et al. Plasma metabolomic and lipidomic alterations associated with COVID-19. *Natl Sci. Rev.* **7**, 1157–1168 (2020).
11. Yamanouchi, T. et al. Origin and disposal of 1,5-anhydroglucitol, a major polyol in the human body. *Am. J. Physiol.* **263**, 268–273 (1992).
12. Nakamura, S., Tanabe, K., Yoshinaga, K., Shimura, F. & Oku, T. Effects of 1,5-anhydroglucitol on postprandial blood glucose and insulin levels and hydrogen excretion in rats and healthy humans. *Br. J. Nutr.* **118**, 81–91 (2017).
13. Zhou, H. & Hylemon, P. B. Bile acids are nutrient signaling hormones. *Steroids* **86**, 62–68 (2014).
14. Ouzir, M., Bouhaddou, N., Khalki, H. & Lakhdar-Ghazal, N. Physiological and pharmacological properties of 5-methoxytryptophol. *Expert Rev. Endocrinol. Metab.* **8**, 355–364 (2013).
15. Yamada, H., Wakamori, S., Hirokane, T., Ikeuchi, K. & Matsumoto, S. Structural revisions in natural ellagitannins. *Molecules* **23**, 1901 (2018).
16. Sams, C. Urinary naphthol as a biomarker of exposure: results from an oral exposure to carbaryl and workers occupationally exposed to naphthalene. *Toxicol.* **5**, 3 (2017).
17. Shimshoni, J. A. et al. Stereoselective formation and metabolism of 4-hydroxy-retinoic acid enantiomers by cytochrome p450 enzymes. *J. Biol. Chem.* **287**, 42223–42232 (2012).
18. Dungan, K. M. 1,5-anhydroglucitol (GlycoMark) as a marker of short-term glycemic control and glycemic excursions. *Expert Rev. Mol. Diagn.* **8**, 9–19 (2008).
19. Zhu, L. et al. Association of blood glucose control and outcomes in patients with COVID-19 and pre-existing type 2 diabetes. *Cell Metab.* **31**, 1068–1077 (2020).
20. Organization, W. H. Definition and diagnosis of diabetes mellitus and intermediate hyperglycemia: reported of a WHO/IDF consultation. *Geneva World Health Organization* (2006).
21. Dworacka, M. et al. 1,5-Anhydro-D-glucitol: a novel marker of glucose excursions. *Int J. Clin. Pr. Suppl.* **129**, 40–44 (2002).
22. Welter, M. et al. Data for serum 1,5 anhydroglucitol concentration in different populations. *Data Brief.* **20**, 753–760 (2018).
23. Bojkova, D. et al. Proteomics of SARS-CoV-2-infected host cells reveals therapy targets. *Nature* **583**, 469–472 (2020).
24. Morita, M. & Akanuma, H. Distribution of 1,5-anhydro-D-glucitol in normal, diabetic, and perfused rat bodies. *J. Biochem.* **112**, 385–388 (1992).
25. Trypsteen, W., Van Cleemput, J., Snippenberg, W. V., Gerlo, S. & Vandekerckhove, L. On the whereabouts of SARS-CoV-2 in the human body: a systematic review. *PLoS Pathog.* **16**, e1009037 (2020).
26. Hoffman, A. M. Bronchoalveolar lavage: sampling technique and guidelines for cytologic preparation and interpretation. *Vet. Clin. North Am. Equine Pr.* **24**, 423–435 (2008).
27. Icard, P. & Saumon, G. Alveolar sodium and liquid transport in mice. *Am. J. Physiol.* **277**, 1232–1238 (1999).
28. Jong, P. M., Sterkenburg, M. A., Kempenaar, J. A., Dijkman, J. H. & Ponc, M. Serial culturing of human bronchial epithelial cells derived from biopsies. *Vitr. Cell Dev. Biol. Anim.* **29**, 379–387 (1993).
29. Bridges, J. P., Vadar, E. K., Huang, H. & Mason, R. J. Respiratory epithelial cell responses to SARS-CoV-2 in COVID-19. *Thorax* **77**, 203–209 (2022).
30. Miki, Y. et al. Evaluation of serum and urine 1,5-anhydro-D-glucitol and myoinositol concentrations in healthy dogs. *J. Vet. Med. Sci.* **73**, 1117–1126 (2011).
31. Codo, A. C. et al. Elevated glucose levels favor SARS-CoV-2 infection and monocyte response through a HIF-1 α glycolysis-dependent axis. *Cell Metab.* **32**, 437–446 (2020).
32. Szczepanski, A. et al. Canine respiratory coronavirus, bovine coronavirus, and human coronavirus OC43: receptors and attachment factors. *Viruses* **11**, 328 (2019).
33. Xia, S. et al. Fusion mechanism of 2019-nCoV and fusion inhibitors targeting HR1 domain in spike protein. *Cell Mol. Immunol.* **17**, 765–767 (2020).
34. Hoffmann, M. et al. SARS-CoV-2 cell entry depends on ACE2 and TMPRSS2 and is blocked by a clinically proven protease inhibitor. *Cell* **181**, 271–280 (2020).
35. Xia, S. et al. Inhibition of SARS-CoV-2 (previously 2019-nCoV) infection by a highly potent pan-coronavirus fusion inhibitor targeting its spike protein that harbors a high capacity to mediate membrane fusion. *Cell Res.* **30**, 343–355 (2020).
36. Ruiz, M. et al. Evolutionarily conserved long-chain Acyl-CoA synthetases regulate membrane composition and fluidity. *eLife* **8**, e47733 (2019).
37. Altmann, D. M., Boyton, R. J. & Beale, R. Immunity to SARS-CoV-2 variants of concern. *Science* **371**, 1103–1104 (2021).
38. Gupta, R. K. Will SARS-CoV-2 variants of concern affect the promise of vaccines? *Nat. Rev. Immunol.* **21**, 340–341 (2021).
39. Alpers, C. E. & Hudkins, K. L. Mouse models of diabetic nephropathy. *Curr. Opin. Nephrol. Hypertens.* **20**, 278–284 (2011).
40. Roesler, W. J., Pugazhenthii, S. & Khandelwal, R. L. Hepatic glycogen metabolism in the db/db mouse. *Mol. Cell. Biochem.* **92**, 99–106 (1990).
41. Meng, X. et al. 1,5-anhydroglucitol attenuates cytokine release and protects mice with type 2 diabetes from inflammatory reactions. *Int J. Immunopathol. Pharm.* **23**, 105–119 (2010).
42. Kato, A. et al. Protective effects of dietary 1,5-anhydro-D-glucitol as a blood glucose regulator in diabetes and metabolic syndrome. *J. Agric. Food Chem.* **61**, 611–617 (2013).
43. Price, D. N. & Muttill, P. Delivery of therapeutics to the lung. *Methods Mol. Biol.* **1809**, 415–429 (2018).
44. Sun, S. et al. Characterization and structural basis of a lethal mouse-adapted SARS-CoV-2. *Nat. Commun.* **12**, 5654 (2021).
45. Shen, B. et al. Proteomic and metabolomic characterization of COVID-19 patient sera. *Cell* **182**, 59–72 (2020).
46. Danlos, F. X. et al. Metabolomic analyses of COVID-19 patients unravel stage-dependent and prognostic biomarkers. *Cell Death Dis.* **12**, 258 (2021).
47. Morita, M. et al. The lipid mediator protectin D1 inhibits influenza virus replication and improves severe influenza. *Cell* **153**, 112–125 (2013).
48. Luo, L. et al. Chenodeoxycholic acid from bile inhibits influenza A virus replication via blocking nuclear export of viral ribonucleoprotein complexes. *Molecules* **23**, 3315 (2018).
49. Kim, Y. & Chang, K. O. Inhibitory effects of bile acids and synthetic farnesoid X receptor agonists on rotavirus replication. *J. Virol.* **85**, 12570–12577 (2011).
50. Yan, H. et al. Sodium taurocholate cotransporting polypeptide is a functional receptor for human hepatitis B and D virus. *eLife* **1**, e00049 (2012).
51. Marcello, A. et al. The cholesterol metabolite 27-hydroxycholesterol inhibits SARS-CoV-2 and is markedly decreased in COVID-19 patients. *Redox Biol.* **36**, 101682 (2020).
52. Civra, A. et al. 25-Hydroxycholesterol and 27-hydroxycholesterol inhibit human rotavirus infection by sequestering viral particles into late endosomes. *Redox Biol.* **19**, 318–330 (2018).
53. Cagno, V. et al. Inhibition of herpes simplex-1 virus replication by 25-hydroxycholesterol and 27-hydroxycholesterol. *Redox Biol.* **12**, 522–527 (2017).
54. Civra, A. et al. Inhibition of pathogenic non-enveloped viruses by 25-hydroxycholesterol and 27-hydroxycholesterol. *Sci. Rep.* **4**, 7487 (2014).
55. Hardison, R. L. et al. Residual antimicrobial coating efficacy against SARS-CoV-2. *J. Appl. Microbiol.* **132**, 3375–3386 (2022).
56. Leist, S. R. et al. A mouse-adapted SARS-CoV-2 induces acute lung injury and mortality in standard laboratory mice. *Cell* **183**, 1070–1085 (2020).
57. Morris, G. M. et al. AutoDock4 and AutoDockTools4: automated docking with selective receptor flexibility. *J. Comput. Chem.* **30**, 2785–2791 (2009).
58. Devkota, R. et al. The adiponectin receptor AdipoR2 and its *Caenorhabditis elegans* homolog PAQR-2 prevent membrane rigidification by exogenous saturated fatty acids. *PLoS Genet.* **13**, e1007004 (2017).

Acknowledgements

We thank the Metabolomics Facility Center of Metabolomics and Lipidomics in National Protein Science Technology Center of Tsinghua University for LC–MS/MS experiments. We thank the core facilities of the Center for Life Sciences and Center of Biomedical Analysis for technical assistance (Tsinghua University). We thank the assistance of Protein Preparation and Identification Facility at Technology Center for Protein Science of Tsinghua University. We thank Y. Xiang from Tsinghua University for his assistance in protein purification and ELISA experiment. We thank J. Qiu for consultation about statistical analysis. We thank X. Zhou from Wuhan University and T. Guo from Westlake University for their assistance in providing information about the raw data of healthy donors and patients with COVID-19. This work was funded by grants from the National Natural Science Foundation of China (32188101, 81961160737, 31825001, 81730063, 8191101056, 82041006 and 31700148) to G.C. and 82102389 to Y.B.Z. The National Key Research and Development Plan of China (2021YFC2300200, 2020YFC1200104, 2018YFA0507202) to G.C. and 2017ZX10304402 to G.Y.Z. Tsinghua University Spring Breeze Fund (2020Z99CFG017), Shenzhen Science and Technology Project (JSGG20191129144225464) and Shenzhen San-Ming Project for Prevention and Research on Vector-borne Diseases (SZSM201611064) to G.C. Innovation Team Project of Yunnan Science and Technology Department (202105AE160020) and the Yunnan Cheng Gong expert workstation (202005AF150034) to G.C. Young Elite Scientists Sponsorship Program (2021QNRC001) to Y.B.Z.

Author contributions

G.C. designed the experiments and wrote the manuscript. L.Q.T. and X.P.X. performed the majority of the experiments and analyzed data. M.L., G.Y.Z., X.Y., D.Y.T., W.J.L., W.B.T., S.Y.F., X.L.H. and S.H.S. helped with the animal experiment. R.L.Z., C.L.W., F.Y., S.S.F., J.S. and J.C.Z. provided the human serum and helped with the work in BSL-3. L.M.Z. helped with bioinformatics analysis. Y.H.L. and X.H.L. helped with metabolic data analysis. L.L., J.Q., N.Z.Z. and S.M.L. provided the bronchiolar epithelial cultures

and contributed to the bronchiolar epithelial cultures staining investigation. L.W. provided the spike full-length protein and helped with ELISA experiment. E.H.M., Y.B.Z., L.Y., H.Z. and P.H.W. contributed experimental suggestions and strengthened the writing of the manuscript. All authors reviewed, critiqued and provided comments to the text.

Competing interests

The authors declare no competing interests.

Additional information

Extended data is available for this paper at <https://doi.org/10.1038/s42255-022-00567-z>.

Supplementary information The online version contains supplementary material available at <https://doi.org/10.1038/s42255-022-00567-z>.

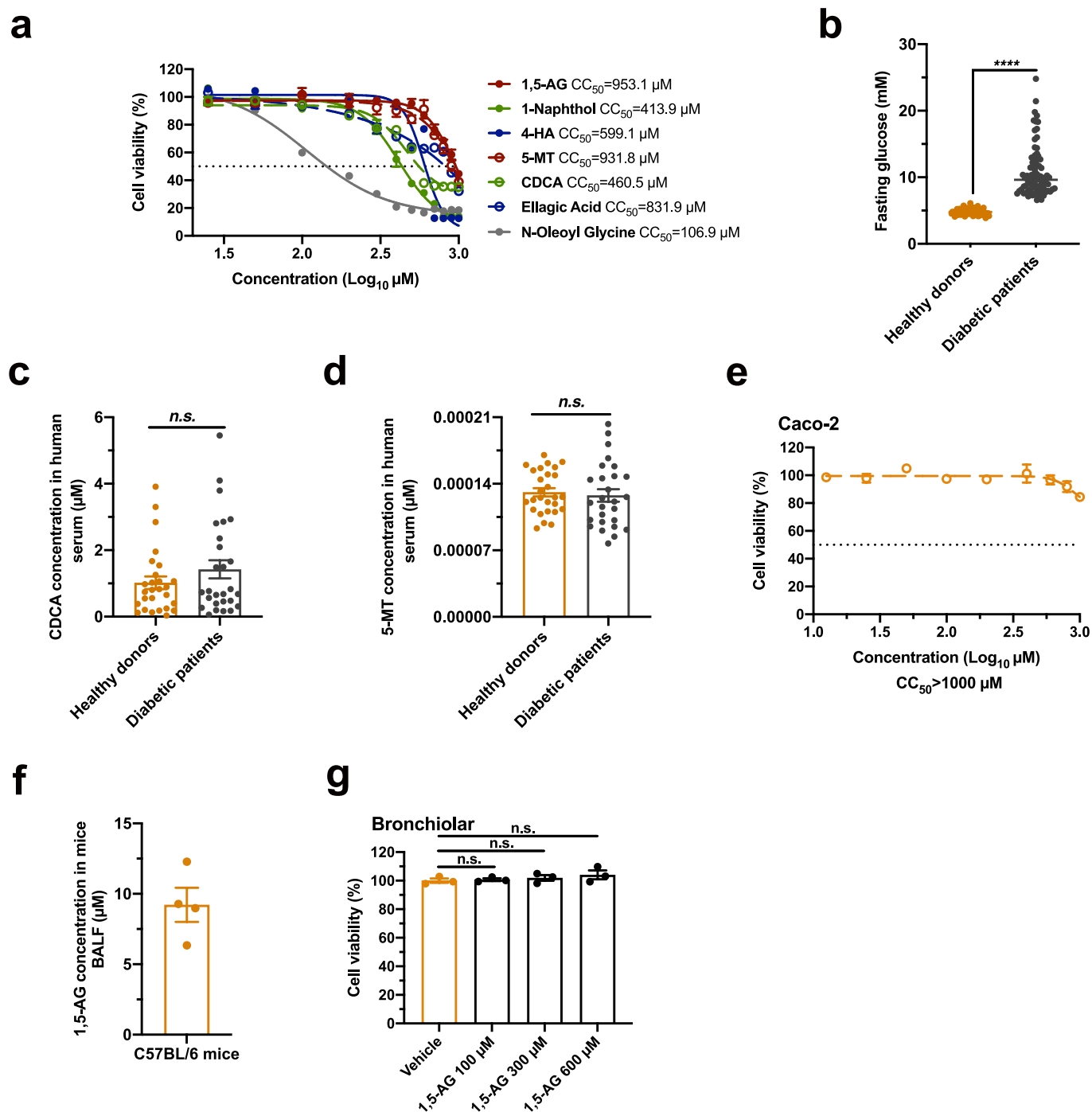
Correspondence and requests for materials should be addressed to Liang Li, Guangyu Zhao, Renli Zhang or Gong Cheng.

Peer review information *Nature Metabolism* thanks Carla F Kim, Nuria Izquierdo-Useros and the other, anonymous, reviewers for their contribution to the peer review of this work. Primary Handling Editor: Alfredo Giménez-Cassina

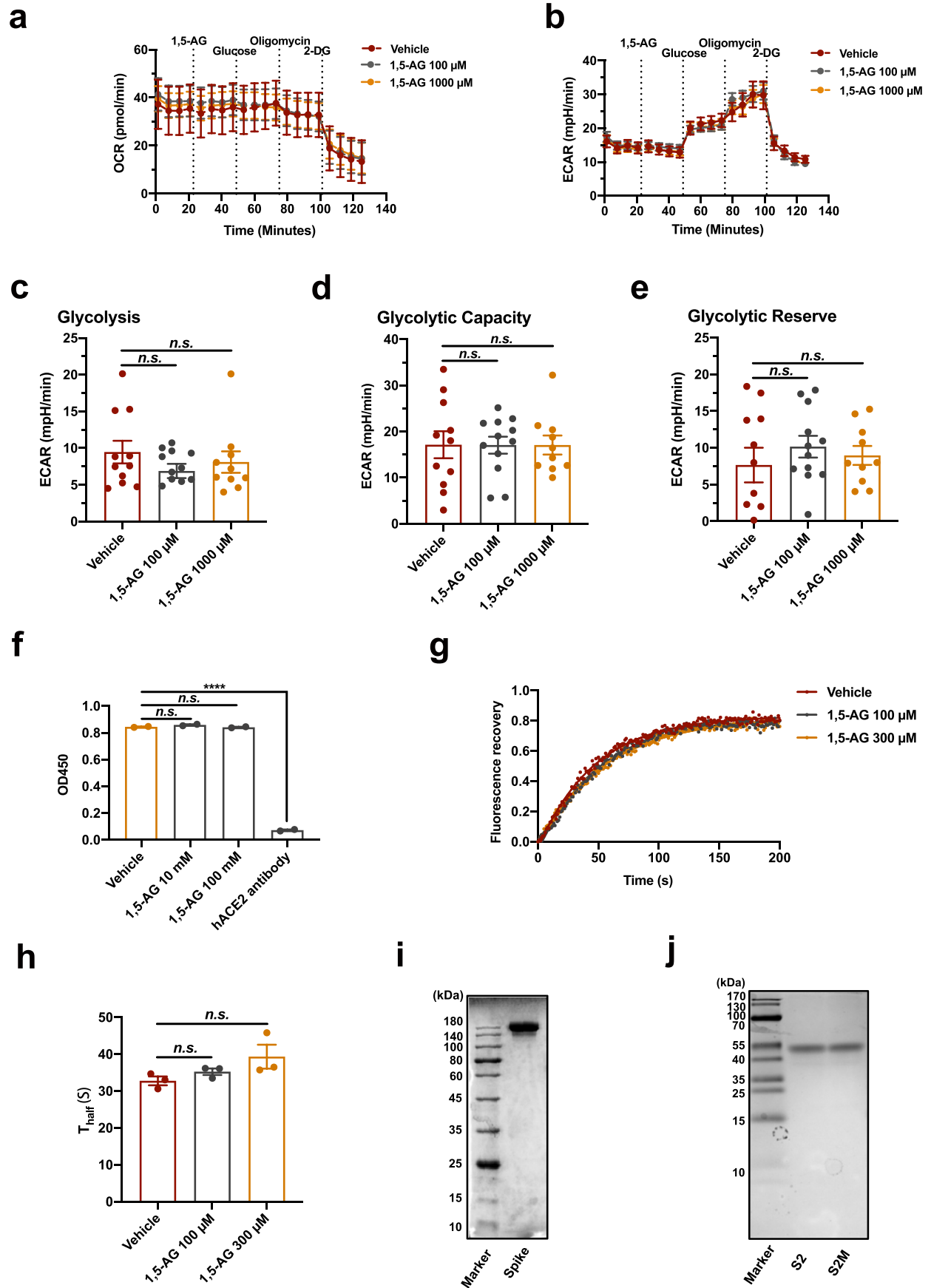
Reprints and permissions information is available at www.nature.com/reprints.

Publisher's note Springer Nature remains neutral with regard to jurisdictional claims in published maps and institutional affiliations.

© The Author(s), under exclusive licence to Springer Nature Limited 2022



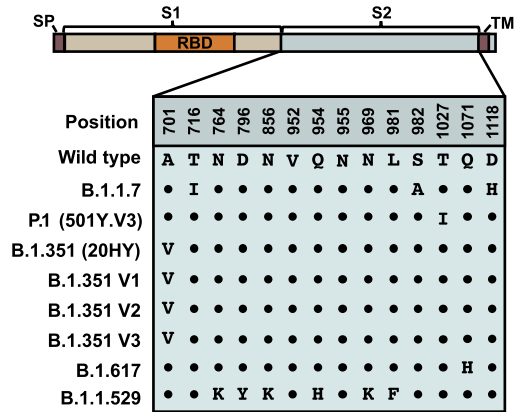
Extended Data Fig. 1 | Characteristics of candidate metabolic component(s). **(a)** Cytotoxicity of 7 identified human metabolites in Vero cells. Cell viability was measured by the CCK-8 assay ($n=4$ biologically independent samples). The gray dotted line represents the value of 50% cell viability. The data are presented as the means \pm S.E.M. **(b)** The hyperglycemia in patients with diabetes' serum. The concentration of fasting serum glucose was measured using the Cobas 8000 modular analyzer (Roche). The horizontal line is the median value. Each dot represents one donor ($n=80$ healthy donors and $n=79$ diabetic patients). $P<0.0001$ for healthy controls versus diabetic patients. **(c, d)** Assessment of CDCA and 5-MT concentrations in the serum of patients with diabetes and healthy donors. The concentrations of CDCA **(c)** and 5-MT **(d)** in the serum were measured using LC-MS/MS. The data are presented as the means \pm S.E.M. Each dot represents one donor ($n=27$ healthy donors and $n=27$ diabetic patients). **(e)** Cytotoxicity of 1,5-AG in Caco-2 cells. The data are presented as the means \pm S.E.M. The gray dotted line represents the value of 50% cell viability ($n=3$ biologically independent samples). **(f)** The concentration of 1,5-AG in the BALF of C57BL/6 J mice. Each dot represents one mouse ($n=4$ mice). The data are presented as the means \pm S.E.M. **(g)** Cytotoxicity of 1,5-AG in human bronchiolar epithelium cultures. The data were analyzed using two-tailed Student's t -test. P values were adjusted using Dunnett's test to account for multiple comparisons. Each dot represents a bronchiolar epithelial culture ($n=3$ bronchiolar epithelial cultures per group). **(b-d)** The data were analyzed using a non-parametric Mann-Whitney U test. **(a, e-g)** Experiments were performed independently at least three biological replicates with comparable results.



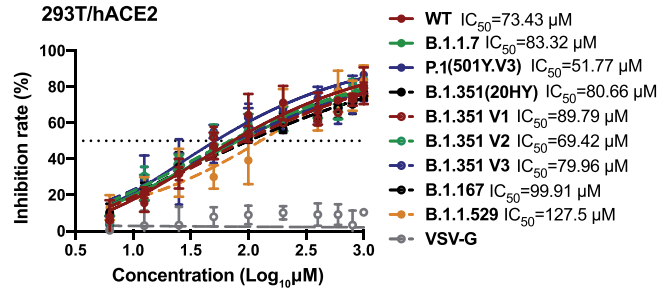
Extended Data Fig. 2 | See next page for caption.

Extended Data Fig. 2 | Incubation with 1,5-AG did not affect the cell glycolysis and membrane fluidity. **(a-e)** Incubation with 1,5-AG did not affect glycolysis in Vero cells. **(a-b)** Vero cells incubated with or without 1,5-AG were exploited to measure the O₂ consumption rate (OCR) **(a)** and the extracellular acidification rate (ECAR) **(b)** upon glycolytic stress (n=11 vehicle, n=12 1,5-AG 100 μM, n=10 1,5-AG 1000 μM). **(c-e)** Incubation with 1,5-AG did not regulate glycolysis in Vero cells. Each dot represents one cell sample (n=11 vehicle, n=12 1,5-AG 100 μM, n=10 1,5-AG 1000 μM). Glycolysis (following glucose injection) **(c)**, glycolytic capacity (following oligomycin injection) **(d)** and glycolytic reserve (glycolytic capacity; glycolysis) **(e)** were calculated from the extracellular acidification rate (ECAR) analysis. **(f-h)** Incubation with 1,5-AG could not affect the interaction between spike and hACE2 as well as membrane fluidity. **(f)** The interaction between the full-length SARS-CoV-2 spike protein and human ACE2 was evaluated by an ELISA kit. The human ACE2 antibody served as a positive control (n=2 biologically independent samples). $P < 0.0001$ for vehicle versus hACE2 antibody. **(g-h)** Incubation with 1,5-AG did not alter the membrane fluidity of 293 T cells. The membrane fluidity was measured by a fluorescence recovery after photobleaching (FRAP) assay. Incubation with 1,5-AG did not cause a significant change in 293 T cells fluorescence recovery **(g)** and T_{half} **(h)** compared to PBS treatment (n=3 biologically independent samples). **(g)** The data are presented as the mean. **(i-j)** Protein purification. The full-length spike protein **(i)** was expressed and purified in human 293 F cells. The purified protein was detected by an SDS-PAGE gel. **(j)** The peptides of S2 and S2M were expressed and purified in *E. coli*. The trimers of S2 and S2M were detected by a nondenaturing electrophoresis. **(a-f, h)** The data are presented as the means \pm S.E.M. The data were analyzed using two-tailed Student's *t*-test. *P* values were adjusted using Dunnett's test to account for multiple comparisons. **(a-j)** Experiments were performed independently at least three biological replicates with comparable results.

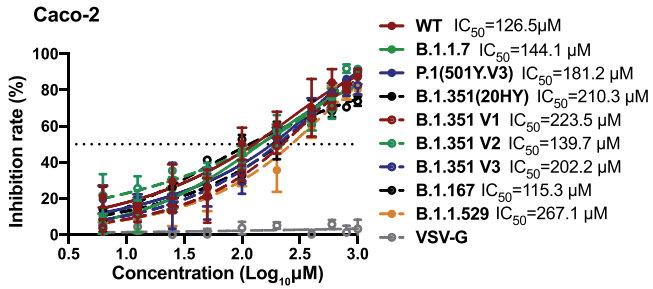
a



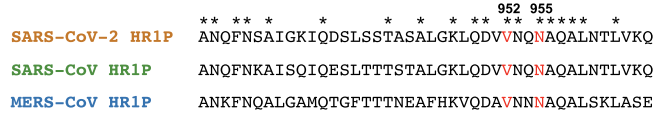
b



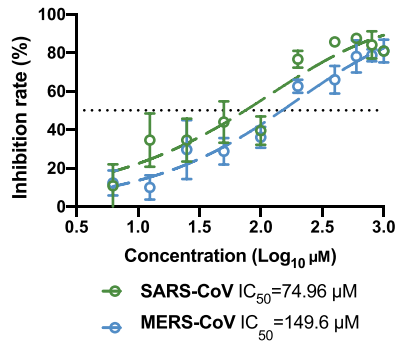
c



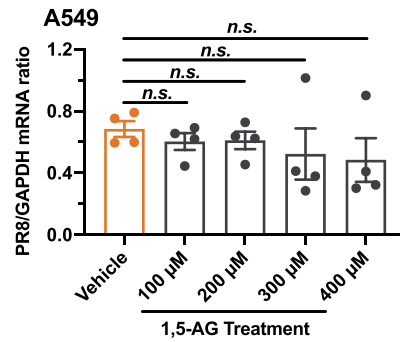
d



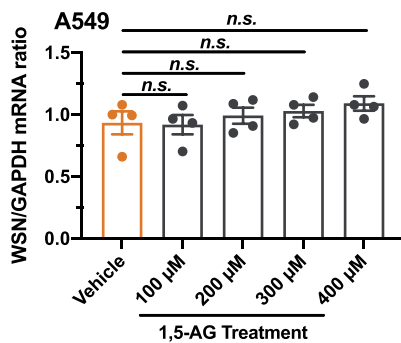
e



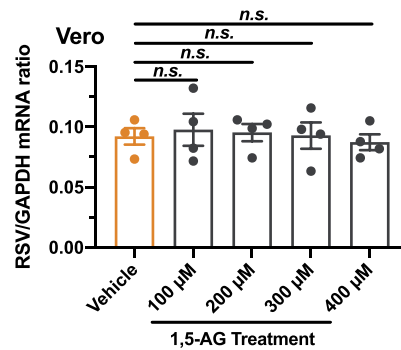
f



g

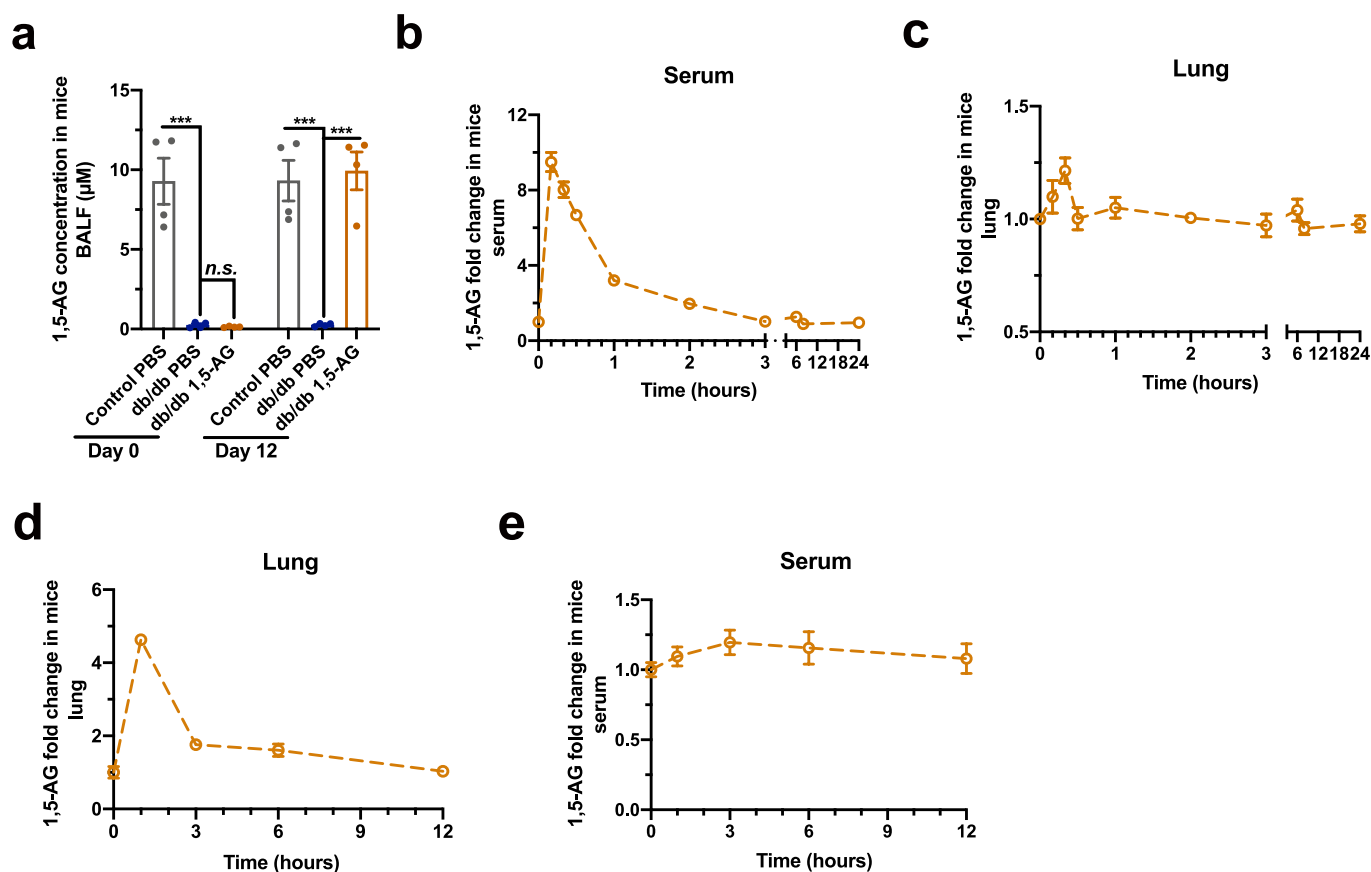


h

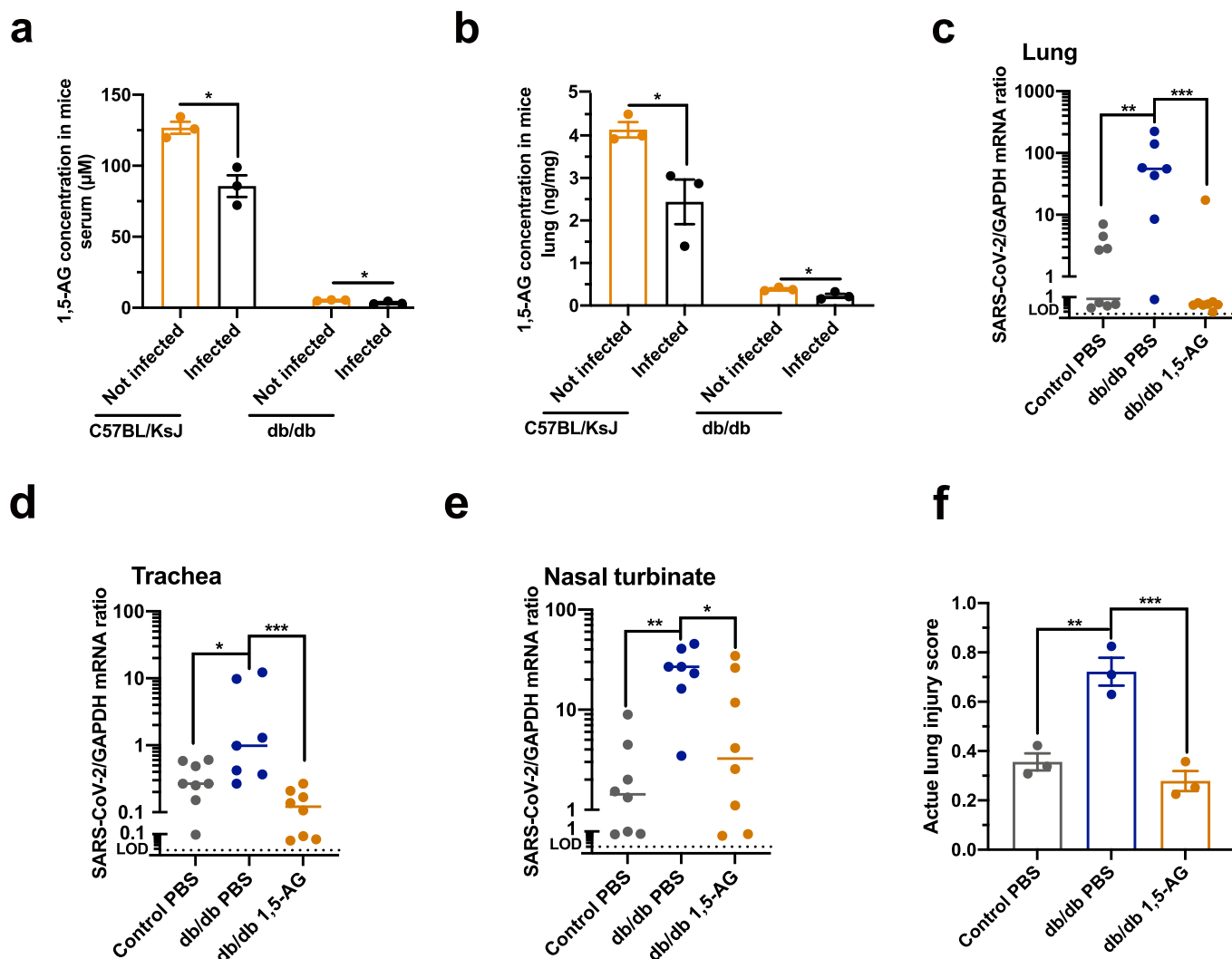


Extended Data Fig. 3 | See next page for caption.

Extended Data Fig. 3 | 1,5-AG inhibited the infections of various coronaviruses. (a-c) 1,5-AG presented general inhibitory activity against the entry process of various SARS-CoV-2 variants. **(a)** The mutation sites in the S2 subunit of the selected SARS-CoV-2 variants with public importance. **(b-c)** 1,5-AG presented general inhibitory activity against the entry process of various SARS-CoV-2 variants into 293 T/hACE2 **(b)** and Caco-2 **(c)** cells. The effectiveness of SARS-CoV-2 spike-mediated viral entry was determined by a luciferase assay ($n=4$ biologically independent samples). The gray dotted line represents the value of 50% inhibition rate. **(d, e)** 1,5-AG inhibited the infections by SARS-CoV and MERS-CoV. **(d)** Comparison of amino acid sequences for the HR1 peptide of SARS-CoV-2, SARS-CoV and MERS-CoV. Asterisks denote identical amino acid residues among all sequences. V952 and N955 are indicated in red. **(e)** 1,5-AG presented general inhibitory activity against the entry process of SARS-CoV in 293 T/hACE2 cells (green line) and MERS-CoV in Huh7 cells (blue line). The effectiveness of spike-mediated viral entry was determined by luciferase assay ($n=4$ biologically independent samples). The gray dotted line represents the value of 50% inhibition rate. **(f-h)** Incubation with 1,5-AG did not influence the infection of the IAV H1N1 PR8 strain **(f)**, WSN strain **(g)** and RSV **(h)** in the tested cells ($n=4$ biologically independent samples). The amount of viral RNA was normalized to human *GAPDH*. **(b-c, e-h)** The data are presented as the means \pm S.E.M. Experiments were performed independently at least three biological replicates with comparable results. **(f-h)** The data were analyzed using two-tailed Student's *t*-test. *P* values were adjusted using Dunnett's test to account for multiple comparisons.



Extended Data Fig. 4 | Metabolic kinetics of 1,5-AG in mice. (a) The concentration of 1,5-AG in mice BALF after pump implantation. The db/db mice with diabetes manifestations were subcutaneously implanted with a 1,5-AG releasing osmotic pump or with a PBS releasing pump as a negative control. The C57BL/KsJ mice treated with a PBS releasing pump were used as a genetic background control. The 1,5-AG concentration was measured in the BALF at 0 and 12 days after pump implantation. The data are presented as the means \pm S.E.M. The data were analyzed using two-tailed Student's *t*-test. *P* values were adjusted using Dunnett's test to account for multiple comparisons. Each dot represents one mouse ($n = 4$ mice per group). $P < 0.0001$ and $P = 0.0003$ for control PBS versus db/db PBS at day 0 and day 12. $P = 0.0002$ for db/db PBS versus db/db 1,5-AG at day 12. (b, c) The metabolic kinetics of 1,5-AG in mice after intravenous administration. The metabolic kinetics of 1,5-AG in mice serum (a) and lung (b). One hundred and twenty-five microliters of 10 mM 1,5-AG were intravenously administered to C57BL/6J mice through the tail vein. (d, e) The metabolic kinetics of 1,5-AG in mice after intra-tracheal administration. The metabolic kinetics of 1,5-AG in mice lung (c) and serum (d). A total of 50 μ l of 10 mM 1,5-AG was aerosolized into C57BL/6J mice using the MicroSprayer Aerosolizer. (b-e) Serum and lung samples were collected at different time points after administration ($n = 3$ mice per group). The concentrations of 1,5-AG in the serum and lung were measured using LC-MS/MS. The data are presented as the means \pm S.E.M. Experiments were performed independently at least three biological replicates with comparable results.



Extended Data Fig. 5 | Restoration of 1,5-AG reduced the SARS-CoV-2 infection in db/db mice detected by qRT-PCR. (a, b) SARS-CoV-2 infection decreased the levels of 1,5-AG in mice serum (a) and lung (b). The mice that were not infected served as controls. The data are presented as the means±S.E.M. The data were analyzed using two-tailed Student's *t*-test. Each dot represents one mouse ($n=3$ mice per group). Experiments were performed independently at least three biological replicates with comparable results. $P=0.0095$ and $P=0.0347$ for non-infected versus infected of C57BL/KsJ and db/db mice serum. $P=0.0377$ and $P=0.0436$ for non-infected versus infected of C57BL/KsJ and db/db mice lung. (c–e) Detection of the SARS-CoV-2 load in the lung (c), trachea (d) and nasal turbinate (e) of infected mice by qRT-PCR. 8,000 p.f.u. of MASCP36 was used for infection per mouse. The horizontal line represents the median value. The data are presented by a logarithmic scale. The gray dotted line represents the value of limit of detection (LOD). The statistical analysis is performed based on log₁₀-transformed values. The viral load was normalized to the mouse *GAPDH*. Each dot represents one mouse ($n=8$ control PBS, $n=7$ db/db PBS and $n=8$ db/db 1,5-AG). $P=0.0056$, $P=0.0157$ and $P=0.0013$ for control PBS versus db/db PBS of lung, trachea and nasal turbinate. $P=0.0003$, $P=0.0003$ and $P=0.0232$ for db/db PBS versus db/db 1,5-AG of lung, trachea and nasal turbinate. (f) Semiquantitative assessment of acute lung injury histological score. Final scores were obtained by averaging three fields per mouse. The data are presented as the means±S.E.M. Each dot represents one mouse ($n=3$ mice per group). $P=0.0021$ for control PBS versus db/db PBS; $P=0.0008$ for db/db PBS versus db/db 1,5-AG. (c–f) The data were analyzed using a non-parametric two-sided Mann-Whitney *U* test. *P* values were adjusted using Dunnett's test. Experiments were performed independently at least three biological replicates with comparable results.

Reporting Summary

Nature Portfolio wishes to improve the reproducibility of the work that we publish. This form provides structure for consistency and transparency in reporting. For further information on Nature Portfolio policies, see our [Editorial Policies](#) and the [Editorial Policy Checklist](#).

Statistics

For all statistical analyses, confirm that the following items are present in the figure legend, table legend, main text, or Methods section.

- | | |
|-------------------------------------|--|
| n/a | Confirmed |
| <input checked="" type="checkbox"/> | <input checked="" type="checkbox"/> The exact sample size (n) for each experimental group/condition, given as a discrete number and unit of measurement |
| <input checked="" type="checkbox"/> | <input checked="" type="checkbox"/> A statement on whether measurements were taken from distinct samples or whether the same sample was measured repeatedly |
| <input checked="" type="checkbox"/> | <input checked="" type="checkbox"/> The statistical test(s) used AND whether they are one- or two-sided
<i>Only common tests should be described solely by name; describe more complex techniques in the Methods section.</i> |
| <input checked="" type="checkbox"/> | <input type="checkbox"/> A description of all covariates tested |
| <input checked="" type="checkbox"/> | <input checked="" type="checkbox"/> A description of any assumptions or corrections, such as tests of normality and adjustment for multiple comparisons |
| <input checked="" type="checkbox"/> | <input checked="" type="checkbox"/> A full description of the statistical parameters including central tendency (e.g. means) or other basic estimates (e.g. regression coefficient) AND variation (e.g. standard deviation) or associated estimates of uncertainty (e.g. confidence intervals) |
| <input checked="" type="checkbox"/> | <input checked="" type="checkbox"/> For null hypothesis testing, the test statistic (e.g. F , t , r) with confidence intervals, effect sizes, degrees of freedom and P value noted
<i>Give P values as exact values whenever suitable.</i> |
| <input checked="" type="checkbox"/> | <input type="checkbox"/> For Bayesian analysis, information on the choice of priors and Markov chain Monte Carlo settings |
| <input checked="" type="checkbox"/> | <input type="checkbox"/> For hierarchical and complex designs, identification of the appropriate level for tests and full reporting of outcomes |
| <input checked="" type="checkbox"/> | <input type="checkbox"/> Estimates of effect sizes (e.g. Cohen's d , Pearson's r), indicating how they were calculated |

Our web collection on [statistics for biologists](#) contains articles on many of the points above.

Software and code

Policy information about [availability of computer code](#)

Data collection	TraceFinder 3.2 (Thermo Scientific), SCIEX OS 1.6, Bio-Rad CFX-96 Touch Real-Time Detection System, Varioskan Flash (Thermo Scientific), Zeiss LSM 880 meta confocal microscope, Seahorse XFe96 Extracellular Flux analyzer (Agilent), Biacore 8K system (GE Healthcare), Olympus FV31S-SW (Olympus).
Data analysis	GraphPad Prism 8.0, Biacore Insight Evaluation software (GE Healthcare), Olympus cellSens software (Olympus), ImageJ (National Institutes of Health).

For manuscripts utilizing custom algorithms or software that are central to the research but not yet described in published literature, software must be made available to editors and reviewers. We strongly encourage code deposition in a community repository (e.g. GitHub). See the Nature Portfolio [guidelines for submitting code & software](#) for further information.

Data

Policy information about [availability of data](#)

All manuscripts must include a [data availability statement](#). This statement should provide the following information, where applicable:

- Accession codes, unique identifiers, or web links for publicly available datasets
- A description of any restrictions on data availability
- For clinical datasets or third party data, please ensure that the statement adheres to our [policy](#)

The numeric source data are provided in source data files and all of the other data that support the findings of this study are available from the corresponding author upon reasonable request. All data generated or analysed during this study are included in this published article (and its supplementary information files).

Field-specific reporting

Please select the one below that is the best fit for your research. If you are not sure, read the appropriate sections before making your selection.

Life sciences Behavioural & social sciences Ecological, evolutionary & environmental sciences

For a reference copy of the document with all sections, see [nature.com/documents/nr-reporting-summary-flat.pdf](https://www.nature.com/documents/nr-reporting-summary-flat.pdf)

Life sciences study design

All studies must disclose on these points even when the disclosure is negative.

Sample size	No statistical methods were used to pre-determine the sample size. Samples sizes were selected based on previous experience to obtain statistical significance and reproducibility.
Data exclusions	The mouse that died before measurement were excluded from the analysis. The criteria was pre-established.
Replication	Experimental findings were reproduced in multiple independent experiments as indicated throughout the manuscript. The times of experimental replication have been provided in the Figure legends. The statistical tests used in this manuscript have been described in both the Statistics section of Methods and the Figure legends.
Randomization	All animals in our experiments were randomly allocated into different groups.
Blinding	The investigators were not blinded to the allocation during the experiments or to the outcome assessment. The data presented did not require the use of blinding.

Reporting for specific materials, systems and methods

We require information from authors about some types of materials, experimental systems and methods used in many studies. Here, indicate whether each material, system or method listed is relevant to your study. If you are not sure if a list item applies to your research, read the appropriate section before selecting a response.

Materials & experimental systems

n/a	Involved in the study
<input type="checkbox"/>	<input checked="" type="checkbox"/> Antibodies
<input type="checkbox"/>	<input checked="" type="checkbox"/> Eukaryotic cell lines
<input checked="" type="checkbox"/>	<input type="checkbox"/> Palaeontology and archaeology
<input type="checkbox"/>	<input checked="" type="checkbox"/> Animals and other organisms
<input type="checkbox"/>	<input checked="" type="checkbox"/> Human research participants
<input checked="" type="checkbox"/>	<input type="checkbox"/> Clinical data
<input checked="" type="checkbox"/>	<input type="checkbox"/> Dual use research of concern

Methods

n/a	Involved in the study
<input checked="" type="checkbox"/>	<input type="checkbox"/> ChIP-seq
<input checked="" type="checkbox"/>	<input type="checkbox"/> Flow cytometry
<input checked="" type="checkbox"/>	<input type="checkbox"/> MRI-based neuroimaging

Antibodies

Antibodies used	All antibodies are commercially available and were commercially validated. Anti-SARS-CoV-2 spike (Supplier: Abcam, Cat: ab273433, clone: 1A9). Western blot: 1: 1000 dilution; immunofluorescence staining: 1:1000 dilution. Anti-SARS-CoV-2 nucleocapsid (Supplier: Abcam, Cat: ab271180, clone: EPR24334-118). Western blot: 1:1000 dilution; immunofluorescence staining: 1:1000 dilution. Anti-Actin (Supplier: Cell Signaling Technology, Cat: 3700, clone: 8H10D10). Western blot: 1:1000 dilution. Anti-hACE2 (Supplier: Abcam, Cat: ab108252, clone: EPR4435(2)). Immunofluorescence staining: 1:1000 dilution. Anti-β-IV-tubulin (Supplier: Abcam, Cat: ab179504, clone: EPR16775). Immunofluorescence staining: 1:1000 dilution. Anti-MUC5AC (Supplier: Abcam, Cat: ab198294, clone: EPR16904). Immunofluorescence staining: 1:1000 dilution. Anti-p63 (Supplier: Abcam, Cat: ab53039, clone: multi-clone). Immunofluorescence staining: 1:500 dilution.
Validation	Based on the catalog number, the information of this commercial antibody, including validation statements, relevant citations and antibody profiles in online databases, is available in the manufacture's website.

Eukaryotic cell lines

Policy information about [cell lines](#)

Cell line source(s)	293T cells (Cat. No# CRL3216), Vero cells (Cat. No# CCL81), Caco-2 cells (Cat. No# HTB37), A549 cells (Cat. No#CCL185), MDCK cells (Cat. No#CCL34), and HepG2 cells (Cat. No# HB8065) were purchased from ATCC. Huh7 cells (Cat. No#JCRB0403)
---------------------	---

	were purchased from JCRB. 293T/hACE2 cells were kindly provided by Prof. Qiang Ding from Tsinghua University.
Authentication	293T cells, Vero cells, Caco-2 cells, A549 cells, MDCK cells, and HepG2 cells have been authenticated using STR.
Mycoplasma contamination	All cells were negative for mycoplasma contamination.
Commonly misidentified lines (See ICLAC register)	No commonly misidentified cell line was used.

Animals and other organisms

Policy information about [studies involving animals](#): [ARRIVE guidelines](#) recommended for reporting animal research

Laboratory animals	Six-week-old male BKS-leprdb (db/db, C57BL/KsJ background) and C57BL/KsJ control mice were purchased from GemPharmatech Co., Ltd. Six-week-old C57BL/6 mice were purchased from Charles River.
Wild animals	The study did not involve wild animals.
Field-collected samples	The study did not involve field-collected samples.
Ethics oversight	The study protocol was approved by the Institutional Animal care and Use Committee at Tsinghua University. All animal experiments involving infectious virus were conducted in Biosafety Level 3 laboratory (BSL-3) and approved by the Animal Experiment Committee of Laboratory Animal Center, Beijing Institute of Microbiology and Epidemiology (approval number: IACUC-IME-2021-017).

Note that full information on the approval of the study protocol must also be provided in the manuscript.

Human research participants

Policy information about [studies involving human research participants](#)

Population characteristics	The blood samples were randomly collected from healthy and diabetic donors signing an informed consent. Human airway biopsies were collected from pulmonary bulla patients with approval of the local ethics committee. We did not collect the other information, such as age, diagnosis history, treatment category.
Recruitment	Human blood was randomly collected from healthy and diabetic donors who provided written informed consent at Tsinghua University and Shenzhen Centers for Disease Control and Prevention. Human airway biopsies were collected with written informed consent from pulmonary bulla patients with approval of the local ethics committee at Shenzhen Institutes of Advanced Technology, Chinese Academy of Sciences, and No.7 Affiliated Hospital of Zhongshan University.
Ethics oversight	Human blood samples were collected with approval of the local ethics committee at Tsinghua University and Shenzhen Centers for Disease Control and Prevention. Human airway biopsies were collected with written informed consent from pulmonary bulla patients with approval of the local ethics committee at Shenzhen Institutes of Advanced Technology, Chinese Academy of Sciences, and No.7 Affiliated Hospital of Zhongshan University.

Note that full information on the approval of the study protocol must also be provided in the manuscript.